

# Large radiation back-flux from Monte Carlo simulations of fusion neutron-material interactions\*

Michael A. Lively<sup>a,b,\*</sup>, Danny Perez<sup>a</sup>, Blas P. Uberuaga<sup>c</sup>, Yanzeng Zhang<sup>a</sup>, Xian-Zhu Tang<sup>a</sup>

<sup>a</sup>Theoretical Division, Los Alamos National Laboratory, Los Alamos, NM, 87545, United States of America

<sup>b</sup>X Computational Physics Division, Los Alamos National Laboratory, Los Alamos, NM, 87545, United States of America

<sup>c</sup>Materials Science and Technology Division, Los Alamos National Laboratory, Los Alamos, NM, 87545, United States of America

---

## Abstract

Fusion power reactors will generate intense neutron fluxes into plasma-facing and structural materials. Radiation back-fluxes, generated from neutron-material interactions under these fluxes, can dramatically impact the plasma dynamics, e.g., by seeding runaway electrons during disruptions via Compton scattering of background electrons by wall-emitted gamma radiation. Here, we quantify these back-fluxes, including neutrons, gamma rays, and electrons, using Monte Carlo calculations for a range of structural material candidates and first wall thicknesses. The radiation back-flux magnitudes are remarkably large, with neutron and gamma radiation back-fluxes on the same order of magnitude as the incident fusion neutron flux. Electron back-fluxes are two orders of magnitudes lower, but are emitted at sufficiently high energies to provide a relatively large back-current through the sheath which may cause sheath reversal. Material configuration plays a key role in determining back-flux magnitudes. The structural material chiefly determines the neutron back-flux magnitude, while the first wall thickness principally attenuates the gamma ray and electron back-fluxes. In addition to prompt back-fluxes, which are emitted immediately after fusion neutrons impact the surface, significant delayed gamma ray and electron back-fluxes arise from nuclear decay processes in the activated materials. These delayed back-flux magnitudes range from 2%–7% of the prompt back-fluxes, and remain present during transients when fusion no longer occurs. During disruptions, build-up of delayed gamma radiation back-flux represents potential runaway electron seeding mechanisms, posing additional challenges for disruption mitigation in a power reactor compared with non-nuclear plasma operations. This work highlights the impact of these radiation back-fluxes plasma performance and demonstrates the importance of considering back-flux generation in materials selection for fusion power reactors.

*Keywords:* fusion neutrons, plasma-material interactions, gamma radiation, electron emission, Monte Carlo

---

## 1. Introduction

In contrast to past and current research devices, burning-plasma operations in future fusion power plants will generate large fluxes of 14.1-MeV fusion neutrons. In ITER, which is expected to achieve 500 MW of sustained fusion power over pulses of  $\sim 400$  s [1], the rate of 14.1-MeV neutron production from D-T fusion would be

$$R_f = \frac{P_f}{E_f} = 1.77 \times 10^{20} \text{ s}^{-1} \quad (1)$$

---

\*This work was supported by the U.S. Department of Energy Office of Fusion Energy Sciences (DOE-FES) [grant number 89233218CNA000001].

\*Corresponding author.

*Email addresses:* [livelym@lanl.gov](mailto:livelym@lanl.gov) (Michael A. Lively), [danny\\_perez@lanl.gov](mailto:danny_perez@lanl.gov) (Danny Perez), [blas@lanl.gov](mailto:blas@lanl.gov) (Blas P. Uberuaga), [yzengzhang@lanl.gov](mailto:yzengzhang@lanl.gov) (Yanzeng Zhang), [xtang@lanl.gov](mailto:xtang@lanl.gov) (Xian-Zhu Tang)

where  $P_f$  is the fusion power of 500 MW, and  $E_f = 17.6$  MeV is the energy released per D-T fusion reaction. Given an estimated plasma-facing surface area  $A_w \sim 660$  m<sup>2</sup>, this equates to an average neutron flux to the walls and divertor of  $\phi_n \sim 2.68 \times 10^{17}$  m<sup>-2</sup> s<sup>-1</sup>. In fusion power reactors with even higher power outputs, the fusion neutron fluxes will approach magnitudes similar to those found in fission power reactors ( $\phi_n \sim 10^{18}$ – $10^{20}$  m<sup>-2</sup> s<sup>-1</sup>), thus posing industrial-scale materials challenges.

To date, fusion neutron-material interactions (NMI) have been investigated from several perspectives. Active NMI research topics include material damage and degradation under neutron irradiation [2–7], tritium breeding [4, 8–12], whole-facility neutron transport for radiation safety [13–16], and radioactive waste generation [10, 17–21]. However, the potential impact of NMI on the plasma performance, principally due to radioactive decay and emission from activated first wall and structural materials, has not yet been investigated, largely because such phenomena are not encountered in non-power-reactor discharges. In this work, we aim to take the first steps towards understanding and characterizing this impact as a basis for evaluating candidate fusion reactor materials.

In practice, NMI in the first wall and structural materials will generate secondary radiation which then transports back to the burning plasma, which we term the *radiation back-flux*. Radiation back-fluxes arise from two major categories of mechanisms: prompt back-fluxes result directly from nuclear and photoatomic collisions, while delayed back-fluxes are those emitted from nuclear decay processes in activated materials. Both categories of back-flux may impact the plasma through several mechanisms, including:

- **Neutron** back-fluxes include secondary and reflected neutrons, which may cross the plasma volume to impact other plasma-facing surfaces and generate additional back-fluxes.
- **Gamma radiation** may seed runaway electrons by Compton scattering of plasma electrons to higher energies [22–24].
- **Electron emission** from photoatomic interactions and/or beta decay, with energies as high as a few MeV, can alter the dynamics of the plasma sheath. These can supply low energy electrons through secondary electron emission when the high energy electrons are brought back to rebombard the wall via electron gyroorbits. The presence of these electrons from the wall can modify the sheath potential, causing qualitative changes in the sheath dynamics [25–27].

In this work, we carry out NMI simulations to characterize the emitted radiation back-fluxes in a fusion power reactor. Furthermore, we elucidate the effect of material design parameters including the first wall thickness and choice of primary structural material. Our simulations show remarkably large radiation back-fluxes, with neutron and gamma radiation back-fluxes in particular being of the same order of magnitude as the incident fusion neutron flux. The high-energy electron back-fluxes are two orders of magnitude lower, but remain substantial enough to impact boundary plasma dynamics. These results highlight the importance of coupled plasma physics/NMI simulations to quantify the impact of the radiation back-fluxes on plasma performance during both steady-state fusion power operations and transient (e.g., disruption) conditions.

## 2. Methods

For our NMI simulations, we use the Monte Carlo N-Particle (MCNP) code, version 6.3.0 [28]. MCNP is a general-purpose radiation transport code which can handle most kinds of particles, including neutrons, photons, electrons, and heavy charged particles. The general simulation setup is shown in Fig. 1. The target material system consists of a tungsten first wall (FW) layer of variable thickness (0.2, 0.5, 2, or 10 mm) atop a one-meter layer of a primary structural material (SM) candidate selected from iron (for comparison purposes), reduced-activation ferritic-martensitic (RAFM) steel [29, 30], Inconel 718 [31], or vanadium alloy [32]. The material compositions are given in Table 1. 14.1-MeV fusion neutrons enter the FW surface at normal incidence. Nuclear data, which describes the complete interactions between the various radiation types and materials, is taken from the ENDF/B-VIII.0 library for neutrons [33, 34], the EPRDATA14 library for photons [35–37], the EL03 library for electrons [38–40], and the ENDF7U library for photonuclear reactions (although these are quite rare in practice) [41, 42].

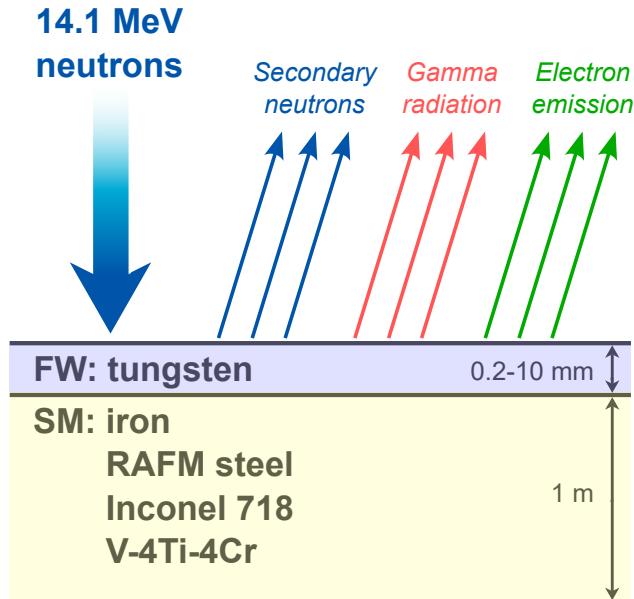


**Fig. 1.** MCNP simulation setup for this work, consisting of 14.1-MeV neutrons incident on a first wall (FW) layer on top of a structural material (SM) layer. Note that arrow positions for the various back-fluxes is schematic only and does not represent an actual spatial distribution of back-fluxes.

Output from the simulation consists of back-fluxes for neutrons, photons, and electrons exiting the FW surface, which are tallied into bins according to the exit energy and time (taking  $t = 0$  at incident neutron arrival). These back-fluxes are normalized to be per incident neutron, and we adhere to this convention in presenting the results throughout this paper. Each MCNP simulation consist of  $10^6$  incident neutron histories. Furthermore, we use the ACT (activation) card to simulate delayed particle emission and transport from nuclear decay of radioactive isotopes resulting from neutron interactions. The full decay solver [43, 44] is quite complex, but consists of two major steps: (1) time-integration of the system of decay equations up to  $10^{10}$ s, and (2) sampling of delayed particle emission from energy distributions given by model physics and/or delayed emission library data. MCNP then simulates the transport of delayed particles as requested by the user.

### 3. Results

Table 2 summarizes the various radiation back-fluxes for each combination of FW thickness and SM selection presented in this work. The most salient features of these results are that:

- Fusion neutron irradiation of reactor materials generates significant radiation back-fluxes, particularly of neutrons and gamma rays. Neutron back-fluxes are of the same order of magnitude as the incident fusion neutron flux, while gamma radiation back-fluxes are within an order of magnitude of the incident flux.
- Material design parameters play a key role in determining the back-flux magnitudes. Neutron back-fluxes depend strongly on the choice of structural material, while the first wall thickness is the dominant factor influencing the gamma ray and electron back-fluxes.
- Delayed gamma ray and electron back-fluxes build up to significant levels during sustained fusion power operations. The terminal delayed gamma ray back-flux magnitude ranges from 2–7% of the prompt back-flux magnitude. These back-flux levels remain substantial enough to influence plasma dynamics during transient, non-fusion events such as disruptions.

Table 1: Material compositions used for MCNP simulations. Elemental concentrations are given in percent atomic (at.%).

Element	First wall	Iron	RAFM steel	Inconel 718	V-4Ti-4Cr
Carbon			0.1	0.08	
Aluminum				0.50	
Silicon			0.1	0.35	
Titanium				0.90	4.0
Vanadium			0.25		balance
Chromium			8.5	19.0	4.0
Manganese			0.5	0.35	
Iron		100	balance	balance	
Cobalt				1.00	
Nickel				52.0	
Copper				0.30	
Niobium				5.00	
Molybdenum				3.00	
Tantalum			0.07		
Tungsten	100		2.0		

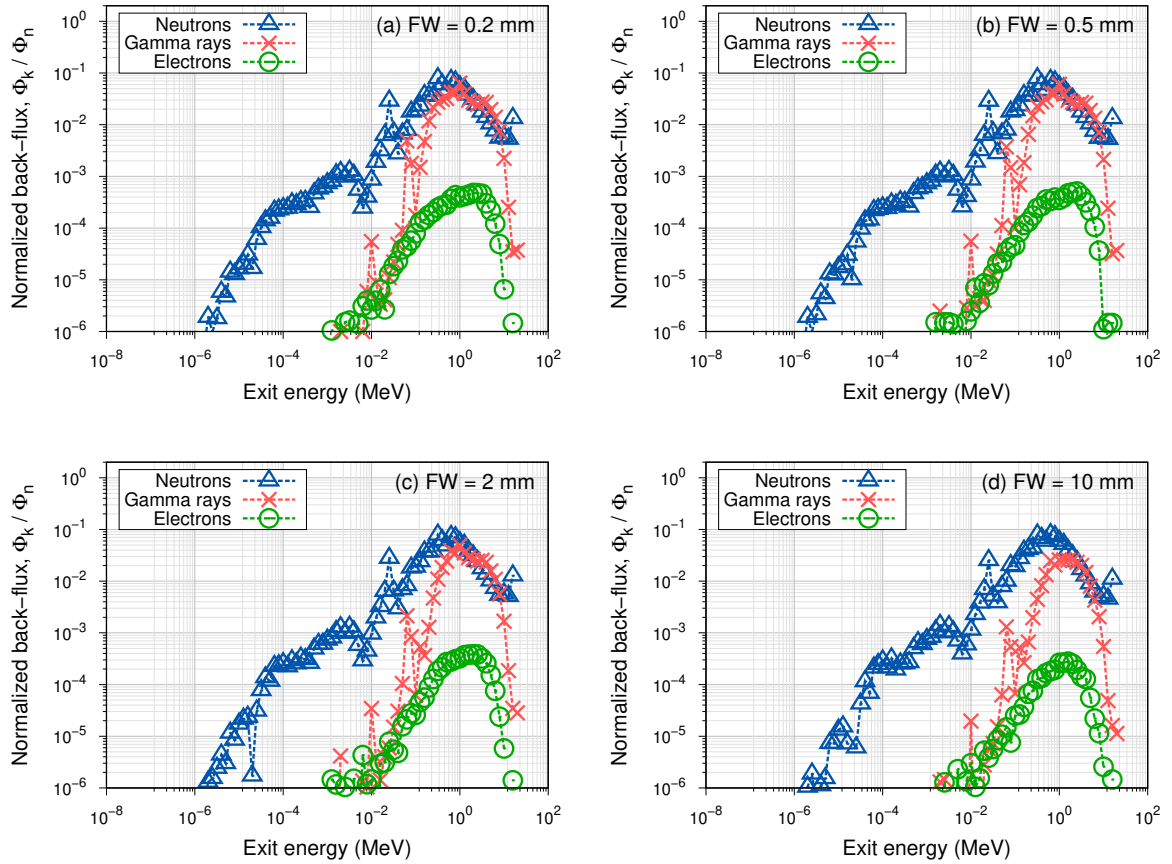
These key outcomes highlight the importance of our results and demonstrate why radiation back-fluxes are a critical topic for fusion power reactor design and operations. In the following sections, we emphasize exemplary results from our simulations to demonstrate clearly each of these points.

Table 2: Summary of radiation back-fluxes from fusion neutron interactions with various material configurations. Fluxes are normalized to the incident neutron flux ( $\phi_n$ ).  $\phi_{n'}$ : total neutron back-flux.  $\phi_{\gamma,p}$ ,  $\phi_{e,p}$ : prompt gamma ray and electron back-fluxes.  $\phi_{\gamma,d}$ ,  $\phi_{e,d}$ : terminal delayed gamma ray and electron back-fluxes.  $\phi_{\gamma,tot}$ ,  $\phi_{e,tot}$ : total gamma ray and electron back-fluxes.

Iron	FW = 0.2 mm	FW = 0.5 mm	FW = 2 mm	FW = 10 mm
$\phi_{n'}$	0.8908	0.8925	0.9006	0.9419
$\phi_{\gamma,p}$	0.5075	0.4667	0.3782	0.2497
$\phi_{\gamma,d}$	0.0165	0.0147	0.0102	0.0032
$\phi_{\gamma,tot}$	0.5239	0.4813	0.3884	0.2530
$\phi_{e,p}$	$5.65 \times 10^{-3}$	$5.58 \times 10^{-3}$	$4.49 \times 10^{-3}$	$2.58 \times 10^{-3}$
$\phi_{e,d}$	$1.30 \times 10^{-4}$	$1.14 \times 10^{-4}$	$8.6 \times 10^{-5}$	$4.7 \times 10^{-5}$
$\phi_{e,tot}$	$5.78 \times 10^{-3}$	$5.69 \times 10^{-3}$	$4.58 \times 10^{-3}$	$2.63 \times 10^{-3}$
RAFM steel	FW = 0.2 mm	FW = 0.5 mm	FW = 2 mm	FW = 10 mm
$\phi_{n'}$	0.8458	0.8480	0.8578	0.9050
$\phi_{\gamma,p}$	0.4895	0.4549	0.3742	0.2491
$\phi_{\gamma,d}$	0.0150	0.0134	0.0094	0.0030
$\phi_{\gamma,tot}$	0.5045	0.4683	0.3836	0.2521
$\phi_{e,p}$	$5.81 \times 10^{-3}$	$5.51 \times 10^{-3}$	$4.31 \times 10^{-3}$	$2.68 \times 10^{-3}$
$\phi_{e,d}$	$1.17 \times 10^{-4}$	$1.06 \times 10^{-4}$	$7.4 \times 10^{-5}$	$3.1 \times 10^{-5}$
$\phi_{e,tot}$	$5.92 \times 10^{-3}$	$5.62 \times 10^{-3}$	$4.38 \times 10^{-3}$	$2.71 \times 10^{-3}$
Inconel 718	FW = 0.2 mm	FW = 0.5 mm	FW = 2 mm	FW = 10 mm
$\phi_{n'}$	0.6292	0.6327	0.6492	0.7301
$\phi_{\gamma,p}$	0.4245	0.3958	0.3298	0.2337
$\phi_{\gamma,d}$	0.0290	0.0250	0.0165	0.0044
$\phi_{\gamma,tot}$	0.4536	0.4209	0.3464	0.2381
$\phi_{e,p}$	$5.19 \times 10^{-3}$	$4.83 \times 10^{-3}$	$3.87 \times 10^{-3}$	$2.50 \times 10^{-3}$
$\phi_{e,d}$	$1.93 \times 10^{-4}$	$1.66 \times 10^{-4}$	$1.05 \times 10^{-4}$	$4.6 \times 10^{-5}$
$\phi_{e,tot}$	$5.38 \times 10^{-3}$	$4.99 \times 10^{-3}$	$3.98 \times 10^{-3}$	$2.55 \times 10^{-3}$
V-4Ti-4Cr	FW = 0.2 mm	FW = 0.5 mm	FW = 2 mm	FW = 10 mm
$\phi_{n'}$	0.9132	0.9137	0.9184	0.9456
$\phi_{\gamma,p}$	0.4504	0.4063	0.3323	0.2532
$\phi_{\gamma,d}$	0.0133	0.0117	0.0084	0.0036
$\phi_{\gamma,tot}$	0.4637	0.4181	0.3407	0.2568
$\phi_{e,p}$	$6.08 \times 10^{-3}$	$5.88 \times 10^{-3}$	$4.85 \times 10^{-3}$	$2.94 \times 10^{-3}$
$\phi_{e,d}$	$1.15 \times 10^{-4}$	$9.8 \times 10^{-5}$	$7.0 \times 10^{-5}$	$4.0 \times 10^{-5}$
$\phi_{e,tot}$	$6.20 \times 10^{-3}$	$5.98 \times 10^{-3}$	$4.92 \times 10^{-3}$	$2.98 \times 10^{-3}$

### 3.1. Prompt radiation back-fluxes in fusion power reactors

Fig. 2 shows radiation back-flux energy distributions for different first wall (FW) thicknesses with RAFM steel as the exemplary structural material (SM). Similar distributions for other considered structural materials are given in the Supplementary Material. Nearly all of the back-fluxes in each plot occur within  $\Delta t \leq 0.1$  ms and is therefore considered prompt. All neutron back-fluxes are prompt (i.e., there is no delayed neutron emission<sup>1</sup>), while for gamma radiation and electron emission the delayed back-fluxes contribute only a few percent of the total magnitude as seen from Table 2. As a rule, this is true for all SM candidates studied in this work. The discussion immediately following therefore chiefly addresses the prompt back-fluxes, while delayed back-fluxes are discussed in Section 3.2.



**Fig. 2.** Energy-resolved, time-integrated radiation back-fluxes of neutrons, gamma rays, and relativistic electrons for RAFM steel structural material with various combinations of tungsten first wall thickness (0.2, 0.5, 2, or 10 mm).

Out of the three radiation types considered, the neutron back-flux is consistently the largest in all cases, ranging from 63% to 95% of the incident fusion neutron flux magnitude. Physically, the neutron back-flux arises from several mechanisms. The high-energy peak between 10 and 14 MeV results from backscattering of incident neutrons by one or a few elastic collisions. The largest, broad peak spanning from  $\sim 50$  keV up to  $\sim 10$  MeV correlates with the energy distribution of secondary neutrons from spallation collisions (that is, collisions leading to ejection of additional neutrons and/or other nuclear fragments). Fig. 3 shows examples

<sup>1</sup>This is very different from the case in a nuclear *fission* reactor, in which delayed neutron emission is not only present but plays a key role in the reactor kinetics.

of these secondary neutron energy distributions extracted from ENDF/B-VIII.0 cross section tables for RAFM steel and tungsten. The peaks of these distributions match well with the broad peaks in the neutron back-flux distributions. At lower energies, around 25 keV, the back-flux distributions show a sharp peak which is specific to the selected SM and most likely corresponds to a nuclear resonance of Fe-56. The same peak appears when pure iron is the SM, while different, smaller peaks appear when Inconel 718 (around 10 keV) or V-4Ti-4Cr (around 60 keV) are the SM. Finally, the neutron back-flux distribution tails off below energies of several keV, a region corresponding to low-energy secondary and reflected neutrons which diffuse out of the wall.

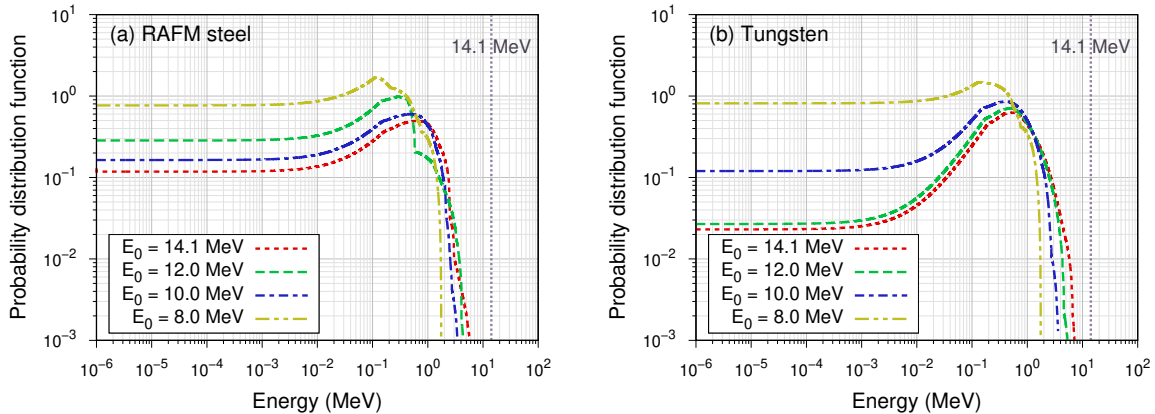
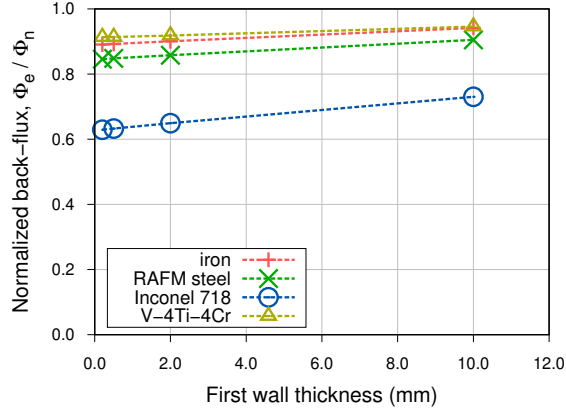


**Fig. 3.** Energy distributions of secondary neutrons from spallation collisions in (a) RAFM steel and (b) tungsten, extracted from ENDF/B-VIII.0 cross section tabular data files [34]. Dashed vertical lines indicate the 14.1 MeV fusion neutron energy as a reference point.

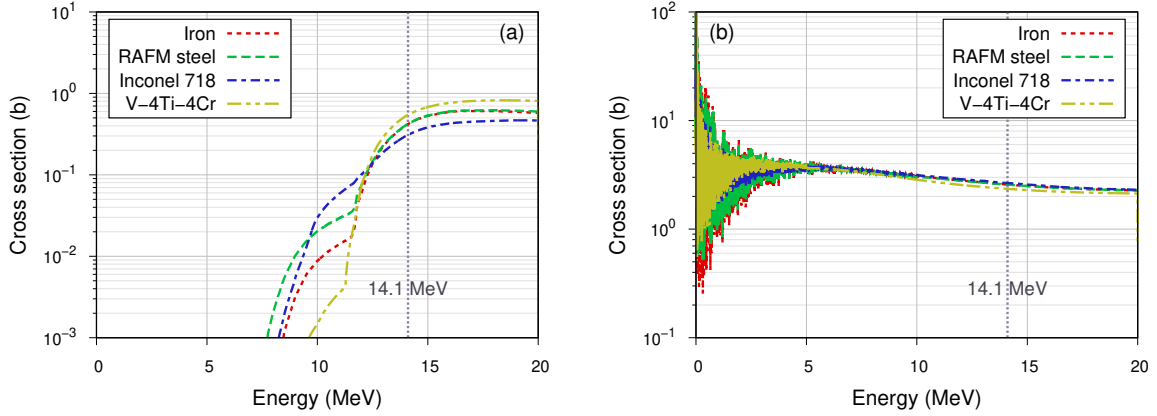
Fig. 4 shows the total neutron back-fluxes for each simulated combination of FW thickness and SM selection. The effect of FW thickness is minor, as for each SM choice the back-flux magnitude increases by  $\sim 10\%$  as FW thickness increases from 0.2 mm to 10 mm. This is due to the greater neutron capture and scattering cross-sections of tungsten compared to the smaller nuclei making up the structural materials. The effect of SM choice is much stronger, as the nickel-based Inconel 718 alloy SM leads to 25–30% lower neutron back-fluxes than the iron, RAFM steel, or vanadium alloy SMs. The strong effect of SM and the weak effect of FW thickness indicate that most neutron scattering and multiplication takes place in the SM rather than the FW.

Fig. 5a shows neutron multiplication cross sections for each SM option, again extracted from the ENDF/B-VIII.0 cross section tabular data files. Based on this, Inconel 718 most likely exhibits lower neutron back-fluxes due to a smaller neutron multiplication cross section at the incident energy of 14.1 MeV. Given this, since V-4Ti-4Cr has an even higher multiplication cross section at the same energy, it is reasonable to ask why the neutron back-flux with the vanadium alloy SM selected is only slightly larger than that for iron-based SMs. To address this question, Fig. 5b shows the total cross sections for each SM option in the same energy range. V-4Ti-4Cr has a lower total cross section than the other SM options between 10 and 14.1 MeV, which means that high-energy neutrons will penetrate more deeply into the vanadium-based material before a collision. On the other hand, for neutron energies of about 2–5 MeV the total cross section in V-4Ti-4Cr is larger on average than that of the other SM options, which means that secondary neutrons emitted in this energy range are more likely to be stopped inside the material. These factors balance out the larger neutron multiplication rate of the vanadium alloy, resulting in a neutron back-flux which is only modestly larger than that for iron-based SMs.

Considering the other radiation types, summarized in Fig. 6, gamma radiation back-fluxes are typically less than the neutron back-fluxes, but within an order of magnitude of the incident fusion neutron flux (see Table 2). Electron emission back-fluxes are consistently around two orders of magnitude lower than



**Fig. 4.** Total neutron back-fluxes summed over all angular and time bins for various combinations of FW thickness and SM selection.



**Fig. 5.** Important cross sections for neutron transport in structural materials, extracted from ENDF/B-VIII.0 cross section tabular data files [34]: (a) neutron multiplication, (b) total cross section. Dashed vertical lines indicate the 14.1 MeV fusion neutron energy as a reference point.

the gamma radiation back-fluxes. Aside from the disparity in magnitudes, gamma radiation and electron emission back-fluxes follow the same trends. This is what we expect: since the primary method for (prompt) electron production is from photoatomic interactions, gamma radiation and electron emission should be closely correlated.

The trends with material parameters for gamma radiation and electron emission back-fluxes are somewhat opposite to the trends for neutron back-fluxes. Specifically, the effect of the SM selection is quite small. On the other hand, the effect of the FW thickness is much more prominent, as the back-flux magnitudes decrease by  $\sim 50\%$  as the FW thickness increases from 0.2 mm to 10 mm. This indicates that the gamma radiation back-flux originates primarily in the SM and is attenuated by passing through the FW, since tungsten with a high atomic number of  $Z = 74$  has much higher photon and electron stopping powers than any alloys based on the first row of transition metals ( $Z = 22$  to  $Z = 29$ ).

### 3.2. Delayed radiation back-fluxes in steady-state fusion power reactors

The delayed back-fluxes, broadly defined to consist of all back-fluxes exiting the wall for  $t > 0.1$  ms, make up only a few percent of the total gamma ray and electron back-fluxes as seen in Table 2 and may be widely distributed over times up to the reactor lifetime ( $\sim 30$  years). Therefore, at first glance the delayed



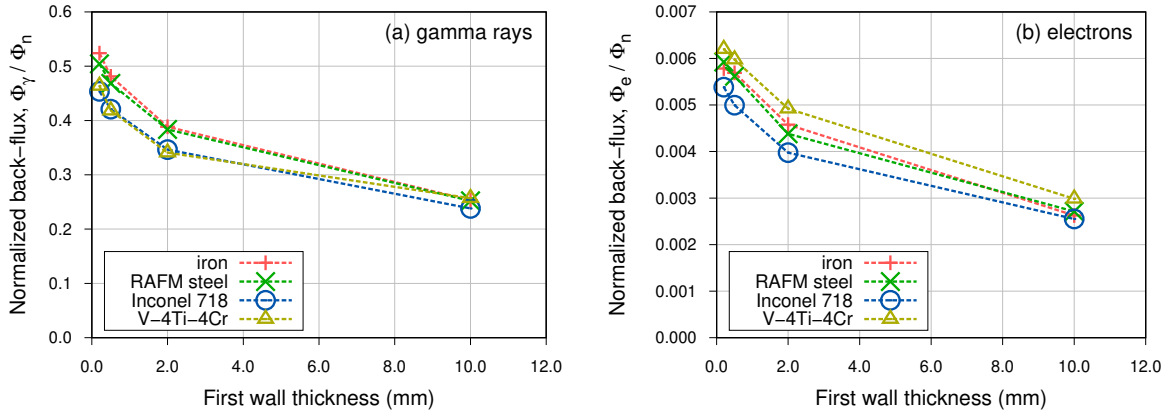


**Fig. 6.** Total (a) gamma and (b) electron radiation back-fluxes out of the simulated wall summed over all time and energy bins.

contributions may seem negligible—this is not the case in reality. In fact, because the delayed back-fluxes are comparatively long-lived, they can build up to potentially significant levels over the course of a fusion reactor’s lifetime. In this section, we show the buildup of delayed back-fluxes and the magnitudes which may be reached over the reactor lifetime.

(Note: we must emphasize that *there is no delayed back-flux of neutrons* in any of our simulations, because none of the transmutation products decay by neutron emission. Only the gamma radiation and electron emission back-fluxes include delayed contributions.)

To begin, let  $\nu(\Delta t - t')$  represent the differential delayed back-flux, with dimensions of  $t^{-1}$  per incident neutron, emitted at time  $\Delta t$  due to a neutron incident at time  $0 \leq t' < \Delta t$  where fusion power operations began at  $t = 0$ . Fig. 7 shows examples of these distributions for delayed gamma rays and electrons for a FW thickness of 2 mm in each case. By assuming steady-state fusion power operations with a constant fusion neutron flux of  $\phi_n$ , we may compute the total delayed back-flux buildup from all incident neutrons during  $0 \leq t \leq \Delta t - t_c$ , where  $t_c = 0.1$  ms is the cutoff time separating prompt and delayed back-fluxes, as

$$\phi_d = \phi_n \int_0^{\Delta t - t_c} \nu(\Delta t - t') dt' \quad (2)$$

We may further consider the worst-case scenario, which is the terminal case as  $\Delta t \rightarrow \infty$  describing the back-fluxes for times beyond the half-life of the longest-lived significant radioisotope. We note that while Eq. (2) assumes a constant  $\phi_n$  for  $0 \leq t \leq \Delta t - t_c$ , a real steady-state fusion power reactor will have down time for maintenance, disruption recovery, etc. This can be represented by multiplying Eq. (2) by a duty factor parameter,  $0 < f_{dc} < 1$  if required. As-is, then, Eq. (2) represents the worst-case scenario for delayed back-flux magnitudes with undisrupted steady-state operations during  $0 \leq t \leq \Delta t - t_c$ .

Fig. 8 shows the integrated back-fluxes of gamma rays and electrons, per incident neutron, for each of the four simulated SMs with a FW thickness of 2 mm in each case. It is immediately apparent that the electron back-fluxes follow the same trends as the gamma ray back-fluxes except for being more than two orders of magnitude smaller. Therefore, in the following discussion the gamma ray and electron delayed back-fluxes are treated together.

The results in Fig. 8 can be assessed for each SM selection:

- With iron as the SM selection, a reactor will reach 86.7% of the terminal back-flux level after 1 day of steady-state fusion power operations. The back-fluxes reach a terminal steady state within 20 years, which is within the nominal reactor lifetime of  $\sim 30$  years. The terminal delayed gamma radiation back-flux magnitude is  $0.0102\phi_n$ , which is 2.7% of the prompt back-flux magnitude.

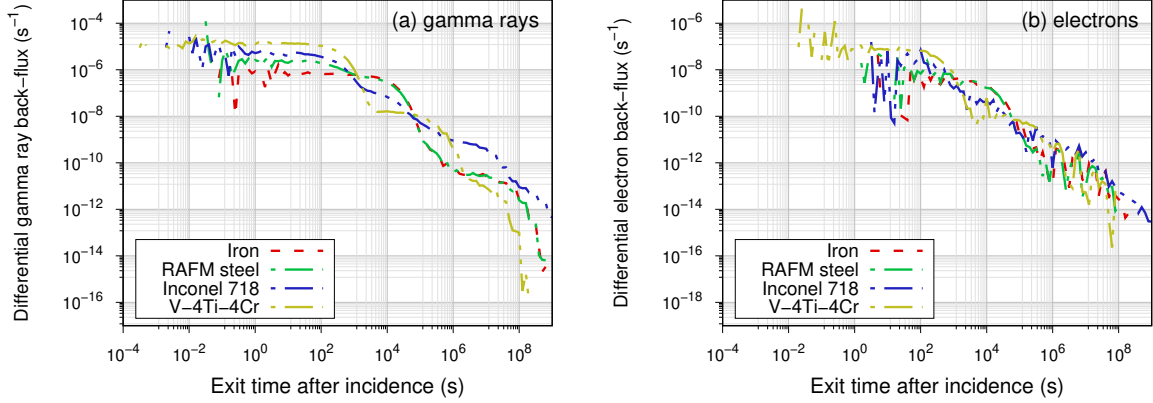


**Fig. 7.** Time-differential delayed back-fluxes,  $\nu(\Delta t - t')$ , of (a) gamma rays and (b) electrons for different structural materials with a 2-mm first wall thickness.

- With RAFM steel as the SM, the behavior is almost identical to that with iron as the SM, except that using RAFM steel leads to a terminal gamma radiation back-flux magnitude of only  $9.4 \times 10^{-3} \phi_n$ , a 7.8% reduction compared to pure iron. This is an expected result, given the reduced-activation nature of RAFM steel, and is attributable to the presence of isotopes which, when activated, form radioisotopes with shorter half-lives than those formed from transmutation of pure iron. The terminal delayed gamma radiation back-flux magnitude in this case is 2.5% of the prompt back-flux magnitude.
- With Inconel 718 as the SM, the comparison with iron-based materials initially looks favorable, as the built-up delayed back-flux magnitude is less than seen from using RAFM steel as the SM for the first 3–4 months of steady-state operations. Beyond this, however, the delayed back-flux magnitude with Inconel 718 is much greater, in large part because no terminal steady state is reached during the nominal 30-year reactor lifetime. The terminal delayed gamma radiation back-flux magnitude in this case is  $0.0165 \phi_n$ , which is 5.0% of the prompt back-flux magnitude. This fraction is much larger than for any other SM selection.
- With V-4Ti-4Cr as the SM, the built-up delayed back-flux is significantly larger for the first few hours of reactor operation, but becomes lower than for the iron-based SM choices after about 3 hours. The built-up delayed back-flux reaches 98.6% of the terminal magnitude after 1 month of operations. The terminal delayed gamma radiation back-flux is  $8.4 \times 10^{-3} \phi_n$ , the lowest level for any SM option in this work and 2.5% of the prompt back-flux magnitude.

Fig. 9 shows the integrated back-fluxes of gamma rays and electrons, per incident neutron, for each of the four simulated FW thicknesses with RAFM steel as the exemplary SM in each case. As was the case for the prompt back-fluxes (c.f. Fig. 6), the FW thickness has a strong attenuation effect. In fact, the FW attenuation is modestly stronger for the delayed back-fluxes than for the prompt ones, as the gamma ray and electron terminal delayed back-fluxes decrease by  $\sim 80\%$  as the FW thickness increases from 0.2 mm to 10 mm, compared to a  $\sim 50\%$  reduction of the prompt back-fluxes over the same domain. This aside, the overall shape of the integrated delayed back-flux curves with increasing fusion operations time is not significantly affected by the FW thickness. This indicates that the delayed back-fluxes originate primarily from decay processes in the SM rather than in the FW, which agrees with the similar conclusion about neutron multiplication drawn from the data in Fig. 4.

While even the largest built-up delayed back-flux level found from these simulations is still  $< 7\%$  of the prompt back-flux level, this few-percent magnitude is significant enough to influence the plasma dynamics under transient conditions when fusion in the plasma stops. In these situations, the prompt back-fluxes disappear but the delayed back-fluxes will remain for a long time. These cases include transients such as

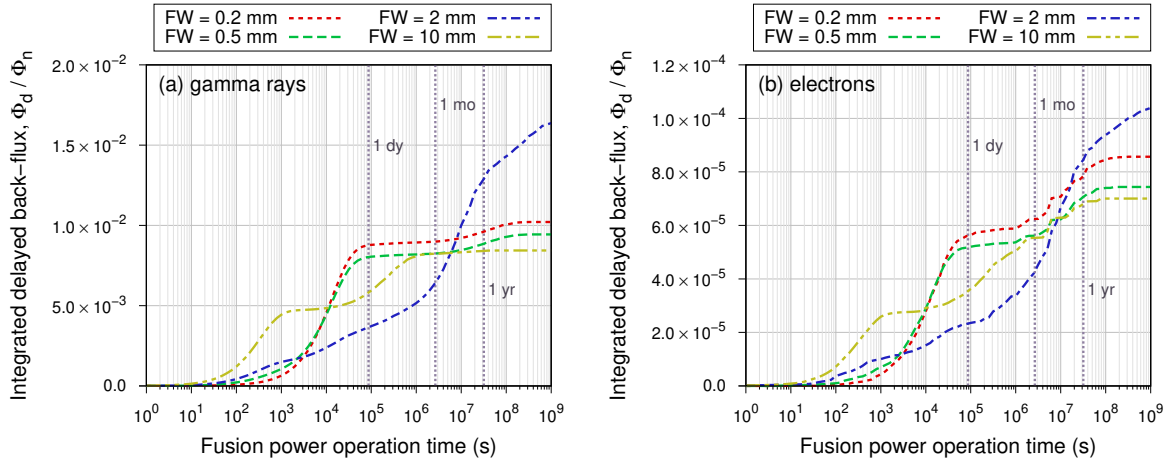


**Fig. 8.** Time-integrated delayed back-fluxes of (a) gamma rays and (b) electrons for different structural materials with a 2-mm first wall thickness.

reactor startup, shutdown, and perhaps most importantly during major disruptions. Most concerning, the build-up of delayed gamma radiation back-flux can drive runaway electron seeding during disruptions via Compton scattering of background electrons, which we discuss below in [Section 4.2](#).

## 4. Discussion

### 4.1. Neutron multiplication impacts

The large neutron back-flux, which is of the same order of magnitude as the incident fusion neutron flux, will transport across the plasma volume and, in most cases, impact on other plasma-facing surfaces. This in turn leads to additional gamma radiation and electron emission back-fluxes caused by these secondary and reflected neutrons (though note that we expect very little to no additional neutron back-flux from this phenomenon, since only 2–3% of the back-flux neutrons are above the threshold energy for neutron multiplication reactions). To characterize the increased back-flux magnitudes, we conducted an additional simulation with a SM of RAFM steel and a FW thickness of 2 mm, in which we added a reflecting boundary for neutrons exiting the FW surface to mimic transport of the neutron back-flux arriving from other hypothetical plasma-facing surfaces. From this simulation, the total gamma radiation back-flux magnitude is  $\phi_{\gamma,\text{tot}} = 0.5431\phi_n$  (an additional 42% over the simulation without a reflecting boundary) and the electron emission back-flux magnitude is  $\phi_{e,\text{tot}} = 6.78 \times 10^{-3}\phi_n$  (an additional 55%). As both of these magnitudes are less than the neutron back-flux (85.8% of incident), a conservative estimate of the additional gamma radiation and electron back-flux magnitudes could be made by multiplying values of  $\phi_{\gamma,\text{tot}}$  and  $\phi_{e,\text{tot}}$  in [Table 2](#) by  $(\phi_n + \phi_{n'})/\phi_n$  in lieu of performing every simulation with the more expensive reflection boundary condition. Of course, in a real fusion reactor the actual back-flux magnitudes will depend on the device geometry.

We also note that many generated secondary neutrons are directed into the material rather than outward as back-flux. Therefore, in a real reactor geometry the flux of secondary neutrons can contribute to the overall neutron flux which reaches the tritium breeding blanket (TBB). Currently, many material candidates have been proposed as neutron multipliers for the TBB [8], including beryllium-based materials such as  $\text{TiBe}_{12}$  [45–48],  $\text{VBe}_{12}$  [47, 49], or  $\text{CrBe}_{12}$  [48], and Pb-based materials such as  $\text{Zr}_5\text{Pb}_3$  [50, 51],  $\text{LaPb}_3$  [52],  $\text{Li}_2\text{Pb}_x\text{Ti}_{1-x}\text{O}_3$  [53]. Choosing the multiplier material which has the optimal combination of thermal, mechanical, and neutronics properties is a daunting challenge for fusion power reactors. The secondary neutron flux towards the TBB should be included in the analysis of these materials, which may allow neutronics requirements to be satisfied more easily and a material with excellent thermal and mechanical

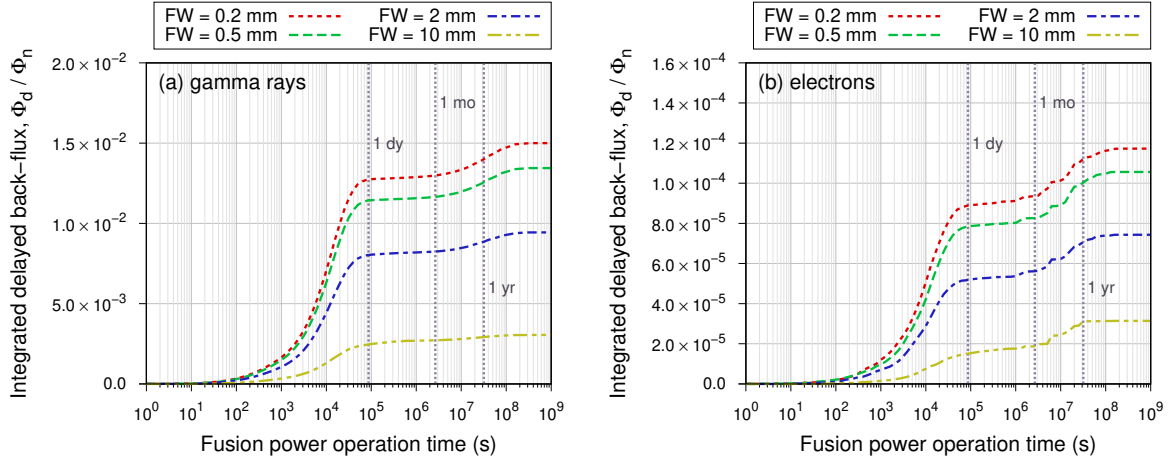


**Fig. 9.** Time-integrated delayed back-fluxes of (a) gamma rays and (b) electrons for different first wall thicknesses with RAFM steel structural material.

properties to be chosen. On the other hand, significant neutron multiplication in non-breeder materials also holds the potential for increased damage production in those materials. Both of these factors should be key considerations in future studied motivated by the present work.

#### 4.2. Compton scattering runaway electron seed from delayed gamma ray back-fluxes

The delayed back-fluxes persist in a fusion power reactor even when fusion is no longer occurring. This is most concerning during a major disruption, when the delayed gamma radiation back-flux can induce a perpetual runaway electron seed through Compton scattering of cold background electrons to high energies. Compton scattering is proposed to be the dominant runaway reseeding mechanism under conditions in which the critical energy,  $W_c$ , for electrons to runaway is high ( $W_c \gtrsim 10$  keV). This can be the case, e.g., after high-Z impurity injection [23, 54, 55], a commonly proposed disruption mitigation method for the thermal quench. While estimates of this Compton seed current have been made previously [22–24], here we carry out a similar estimate to demonstrate the utility of our results to characterize the Compton seed current in terms of the material configuration of a fusion reactor, thus aiding disruption mitigation through materials design and engineering.

While plasma physics simulations of the runaway dynamics are necessary to accurately predict the runaway current induced by Compton scattering, here we can estimate the runaway seed current,

$$I_{\text{seed}} = \dot{n}_{\text{re}} A_{\text{xs}} \tau_{\text{res}} e \langle v_{\text{re}} \rangle f(\xi_c) \quad (3)$$

where  $\dot{n}_{\text{re}}$  is the runaway generation rate by Compton scattering,  $A_{\text{xs}}$  is the cross-sectional area of the plasma volume,  $\tau_{\text{res}}$  is the exponential current quench time constant following [22],  $e$  is the elementary charge,  $\langle v_{\text{re}} \rangle$  is the average speed of a high-energy electron produced from Compton scattering, and  $f(\xi_c)$  is the fraction of Compton scattering electrons with directional cosines  $\xi > \xi_c$  relative to the magnetic field direction (electrons outside of this range will radiate their energy away and will not become runaways). The critical cosine value is defined as  $\xi_c = \sqrt{2a/R_0}$  with  $a$  and  $R_0$  the minor and major tokamak radii, respectively.

The runaway generation rate is computed as

$$\dot{n}_{\text{re}} = n_e \int \sigma_c(E_\gamma) d[\phi_{\gamma,d}(E_\gamma)] \quad (4)$$

with  $n_e$  the nominal electron density and  $\phi_{\gamma,d}(E_\gamma)$  the energy-dependent delayed gamma radiation back-flux distribution. An example of this distribution is given in Fig. 10 and compared to the energy distribution for

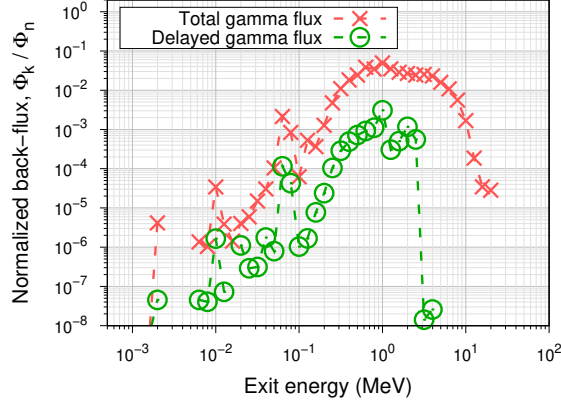


**Fig. 10.** Energy distributions of the total and delayed gamma radiation back-fluxes for RAFM steel with a first wall thickness of 2 mm.

the total (prompt plus delayed) back-flux. The energy distribution of the delayed gamma radiation back-flux is similar to that of the total back-flux, except for a lack of high-energy gamma rays above a few MeV.

The energy-dependent Compton cross section,  $\sigma_c(E_\gamma)$ , is obtained from

$$\sigma_c(E_\gamma) = \int_{\theta_c}^{\pi} \frac{d\sigma}{d\Omega} d\Omega \quad (5)$$

where  $d\Omega = 2\pi \sin \theta d\theta$  and

$$\frac{d\sigma}{d\Omega} = \frac{r_e^2}{2} \frac{E_\gamma'^2}{E_\gamma^2} \left( \frac{E_\gamma}{E_\gamma'} + \frac{E_\gamma'}{E_\gamma} - \sin^2 \theta \right) \quad (6)$$

with  $E_\gamma'$  the energy of the scattered gamma ray and  $\theta$  the scattering angle. A critical value of the scattering angle exists,  $\theta_c$ , which depends on  $E_\gamma$  and must be exceeded to generate an electron with energy greater than  $W_c$ . This is given by [22]

$$\theta_c = \cos^{-1} \left( 1 - \frac{m_e c^2}{E_\gamma} \frac{W_c/E_\gamma}{1 - W_c/E_\gamma} \right) \quad (7)$$

The average velocity of a Compton scattering electron is obtained using Eq. (6) as

$$\langle v_{\text{re}} \rangle = \left\{ \int_{E_\gamma} \int_{\Omega} v_{\text{re}}(\Omega) \frac{d\sigma}{d\Omega} d\Omega d[\phi_{\gamma,d}(E_\gamma)] \right\} / \left\{ \int_{E_\gamma} \int_{\Omega} \frac{d\sigma}{d\Omega} d\Omega d[\phi_{\gamma,d}(E_\gamma)] \right\} \quad (8)$$

where  $v_{\text{re}}(\Omega)$  of a Compton scattering electron may be computed from its recoil energy,  $E_\gamma - E_\gamma'$ .

Finally, we estimate the value of  $f(\xi_c)$  by assuming an isotropic scattering distribution, due to the fact that gamma radiation back-flux is emitted from every plasma-facing surface over a range of exit angles. Thus, we use the simple relation  $f(\xi_c) = \cos^{-1}(\xi_c)/\pi$ .

Fig. 11 gives the results of these calculations ( $I_{\text{seed}}$ ) for each combination of SM choice and FW thickness simulated for this work. For these estimates, we choose an ITER-like geometry ( $R_0 = 6.2$  m,  $a = 2.0$  m, plasma chamber volume  $V = 840$  m<sup>3</sup>, and wall surface area  $A_w = 660$  m<sup>2</sup>), yielding parameter values of  $A_{\text{xs}} = V/(2\pi R_0) = 21.6$  m<sup>2</sup>,  $\xi_c = 0.803$ , and  $f(\xi_c) = 0.203$ . We choose  $W_c = 18.6$  keV, which is the minimum value of  $W_c$  required to eliminate the possibility of runaway seeding by tritium decay. We also choose  $\tau_{\text{res}} = 0.034$  s to allow comparison with some of the results from [22]. We note that the use of  $\tau_{\text{res}}$  in Eq. (4) is an approximation, necessary in the absence of plasma physics simulations, by which we estimate the Compton scattering runaway seed current generated on the same time scale as the

current quench decay time. Finally, we choose representative values of the fusion neutron flux to the wall,  $\phi_n \sim 2.68 \times 10^{17} \text{ m}^{-2}\text{s}^{-1}$ , representing 500 MW of fusion power, and nominal electron density during the disruption of  $n_e = 4 \times 10^{20} \text{ m}^{-3}$  which includes the effect of impurity injection [56]. For this analysis, we use the terminal delayed gamma radiation back-flux levels (as reported in Table 2).

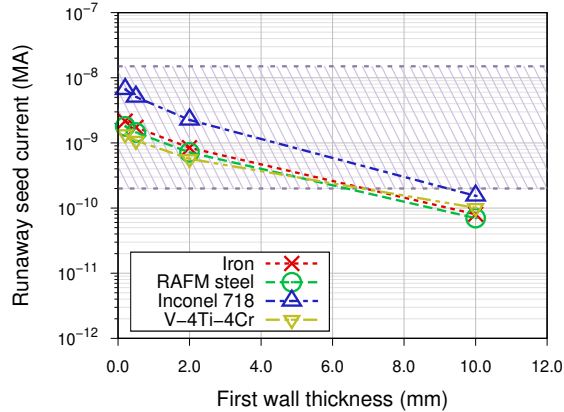


**Fig. 11.** Compton scattering runaway electron seed currents,  $I_{\text{seed}}$  (in MA), estimated from MCNP calculations of delayed gamma radiation back-fluxes for various material configurations. The shaded region depicts the range of Compton seed current values calculated in Fig. 9 of [22].

The runaway seed current data in Fig. 11 highlight the impact of material configuration parameters, as both the FW thickness and SM choice significantly affect the seed current. A sufficient first wall thickness can greatly attenuate the gamma radiation back-flux, particularly the lower-energy gamma rays which have higher Compton scattering cross section values, and thus reduce the runaway seed current accordingly. In particular, increasing the first wall thickness from 2 mm to 10 mm reduces the runaway seed current by a factor of 5 to 10. The choice of structural material has a similarly large effect, most notably the runaway seed current when Inconel 718 is the structural material is consistently larger than that in other cases by a factor of 2 to 5. We also note that different SM choices and FW thicknesses interact to produce a complex variation of  $I_{\text{seed}}$ . For example, V-4Ti-4Cr SM exhibits the lowest runaway seed currents for FW thicknesses of 2 mm or less, but when the FW thickness is 10 mm the iron-based SMs exhibit the lowest seed currents.

We note that the values of  $I_{\text{seed}}$  in Fig. 11 agree well with previous published studies of this topic. Martín-Solís and coworkers calculated Compton runaway seed values ranging from  $2 \times 10^{-10}$  to  $1.5 \times 10^{-8}$  MA [22]. Vallhagen and coworkers performed a similar analysis [23, 24], and reported total runaway seed currents from all mechanisms in the range from  $10^{-12}$  to  $10^{-6}$  MA under a variety of plasma conditions (although Compton-only contributions were not separated in these works). These authors showed that even these apparently small magnitudes of runaway seed current are sufficient to avalanche up to  $\sim$ MA runaway currents which can threaten to damage or destroy reactor components. However, this work used an unrealistically large value of  $\phi_\gamma \sim 10^{18} \text{ m}^{-2}\text{s}^{-1}$  and did not reduce this value to account for the loss of prompt back-flux after the thermal quench.

Comparing the results in Fig. 11 to these literature values indicates the value of the present work. On one hand, the good agreement between our estimates and the wider literature is encouraging, given the only cursory consideration of plasma conditions possible in our estimate. At the same time, we note that the previous calculations were performed using a rough estimate of the gamma radiation back-flux energy spectrum, which is of questionable accuracy (notably, the high-energy tail where  $E_\gamma > 10$  MeV is unphysical) and was computed for a Be first wall but never updated for the planned tungsten first wall. The ready availability of accurate gamma radiation back-flux magnitudes and energy spectra via the simulation approach shown in this work, which can be readily prepared for specific material configurations, enables accurate predictions of the Compton seed current. Therefore, a coupled material-plasma modeling framework to make these calculations on-demand is a key direction for future work.

### 4.3. Electron back-flux impact on sheath dynamics

Finally, electron back-fluxes of  $\sim$ MeV average energies can impact the plasma sheath in several ways, depending on the angular distribution of the emitted electrons and the magnetic incident angle at the wall. Firstly, with a nearly tangential incident angle for the magnetic field at the divertor and first wall, one would expect that the emitted electrons would follow the gyro-orbit and impact the wall surface again. Both high energy backscattered electrons (BSE) and the predominantly low energy secondary emission electrons (SEE) can result from this re-entry of the gyrating electrons into the wall, which could qualitatively modify the sheath behavior from classical models [25–27, 57]. We note that the gyroradius of the high-energy electrons is much larger than that of the low temperature ions in the divertor, so that the Chodura sheath physics [58, 59] should be revisited. Secondly, the high-energy electrons may affect the collisional-radiative physics due to the relativistic enhancement of the collisional excitation and ionization cross sections [60], which can mostly occur near the target surface where the high-energy electrons get trapped. Finally, if the emitted high energy electrons were able slide away along the magnetic field before gyrating back to the wall, their high energies allow a large electron current from the wall emission, which can alter or potentially even reverse the sheath potential [25, 26] despite a lower back-flux magnitude.

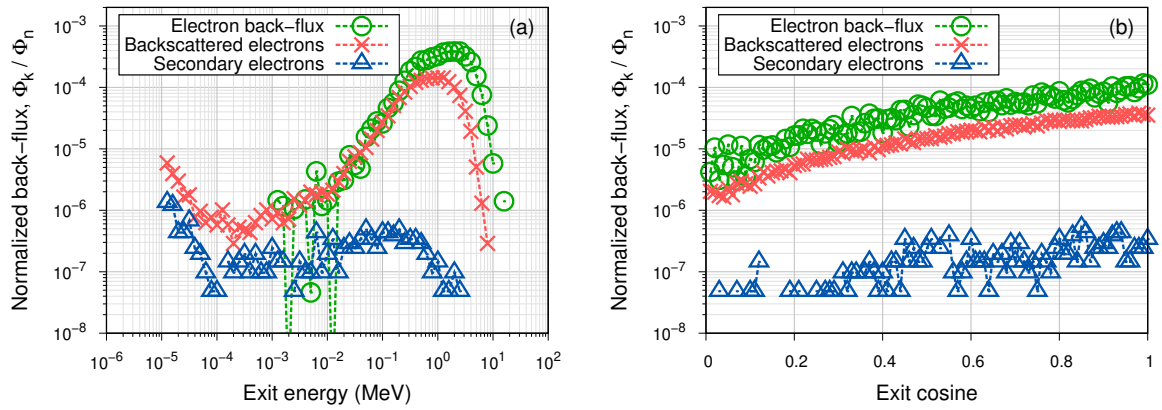


**Fig. 12.** (a) Energy and (b) cosine distributions for electron back-flux (from incident neutrons), backscattered electrons, and secondary electrons (both from backflux rebombardment) emitted from RAFM steel with a 2-mm first wall thickness. Note that the BSE and SEE distributions obtained from MCNP calculations are necessarily incomplete, owing to the 1 keV lower cutoff energy.

While analysis of these potential impacts requires detailed plasma simulations and is beyond the scope of the current work, the energy and angular distributions of the BSEs and SEEs obtained from MCNP calculations are useful results which form the input conditions for plasma simulations. Fig. 12 shows such BSE and SEE energy and cosine distributions exiting the surface obtained by MCNP calculations for RAFM SM with a 2-mm FW thickness, compared against the electron back-flux (from neutron irradiation) for the same material configuration. The simulation setup is same as Fig. 1 except that the normal incident particles are electrons with the same energy distribution as the electron back-flux, e.g., as in Fig. 2c. We must note that the BSE and SEE distributions obtained from MCNP calculations are necessarily incomplete, owing to the absolute lower energy cutoff for electrons in MCNP of 10 eV. The results show that above 10 eV, the backscattering yield is 0.412 BSEs per incident electron, while the secondary emission yield is much smaller at only 0.0034 SEEs per incident electron. In particular, the missing low-energy part of the SEE distribution is likely to contribute significantly to the total SEE fluxes, given that the energy distributions for SEEs increases sharply to a maximum as the energy approaches the 10-eV lower cutoff. Therefore, for complete SEE input to plasma sheath simulations, MCNP calculations must be supplemented by low-energy SEE models [27].

## 5. Conclusion

We have quantified the radiation back-fluxes from fusion neutron irradiation of reactor materials with MCNP simulations. These radiation back-fluxes are remarkably large, with neutron and gamma ray back-fluxes on the same magnitude as the incident fusion neutron flux. Though strongly correlated with the gamma ray back-fluxes, the electron back-fluxes are two orders of magnitude smaller in all cases. The radiation back-fluxes are significantly impacted by the material design parameters. The neutron back-flux depends most strongly on the choice of structural material, while the gamma ray and electron back-flux magnitudes are dominated by the first wall thickness. In addition to prompt back-fluxes, nuclear decay processes in activated reactor materials lead to significant delayed gamma ray and electron back-fluxes. During steady-state fusion power operations, the delayed gamma ray back-flux builds up to a magnitude of 2%–7% of the prompt back-flux magnitude, while the delayed electron back-flux magnitude remains two orders of magnitude lower.

Radiation back-fluxes can have profound impacts on plasma performance and reactor operations. The significant neutron back-flux has the ultimate effect of increasing the gamma radiation and electron emission back-fluxes by  $\sim 50$ – $80\%$ , although in a real reactor this enhancement also depends on the geometry of the plasma-facing surfaces. The substantial neutron back-flux also implies significant neutron multiplication in the first wall and structural materials, which must be considered in the design of tritium breeding blankets and could ease the design constraints of those systems. Furthermore, the build-up over time of delayed gamma radiation back-fluxes during fusion power operations will induce significant runaway electron seeding by Compton scattering of cold plasma electrons, posing significant challenges for disruption mitigation compared to non-nuclear environments. Finally, the electron back-flux of  $\sim$ MeV average energies can impact the plasma sheath in several ways: electrons may be directed back into the surface by the magnetic field, leading to significant backscattering and secondary electron emission fluxes into the sheath, they may drive enhanced excitation and ionization of near the wall, or they may slide away from the wall along the magnetic field, contributing a large electron emission current component which could drastically alter the sheath potential. All of these back-flux phenomena can significantly impact plasma performance in a future fusion power reactor.

We envision two principal avenues for future extension and implementation of this work. First, our simulation methodology should be scaled up to reactor geometries to obtain spatially-dependent radiation back-flux profiles for real devices, including studies of potential TBB designs. Second, the radiation back-flux profiles must be coupled to whole-device plasma physics simulations to elucidate the impact on plasma performance. Such efforts are urgently motivated by the revelation from this work of how impactful the effects of radiation back-fluxes can be. Given the significant potential impact of these formerly overlooked mechanisms on the performance of fusion power reactors, analysis of radiation back-flux effects are of crucial importance to any consideration of reactor engineering and design.

## Acknowledgements

This work is funded by the U.S. Department of Energy Office of Fusion Energy Sciences (DOE-FES) under the Tokamak Disruption Simulation (TDS) Scientific Discovery through Advanced Computing (SciDAC) project at Los Alamos National Laboratory (LANL) under Contract No. 89233218CNA000001. Los Alamos National Laboratory is operated by Triad National Security LLC, for the National Nuclear Security administration of the U.S. DOE under Contract No. 89233218CNA000001.

The authors are grateful to Colin J. Josey for helpful discussion regarding the ACT card in MCNP.

*CRedit author statement.* **Michael A. Lively:** Conceptualization, Methodology, Formal Analysis, Investigation, Writing - original draft, Writing - review & editing, Visualization. **Danny Perez:** Conceptualization, Writing - review & editing. **Blas P. Uberuaga:** Conceptualization, Writing - review & editing. **Yanzeng Zhang:** Conceptualization, Writing - review & editing. **Xianzhu Tang:** Conceptualization, Writing - review & editing, Project administration, Funding acquisition.



## References

- [1] D. J. Campbell, A. Loarte, D. Boilson, X. Bonnin, P. de Vries, L. Giancarli, Y. Gribov, M. Henderson, S. H. Kim, P. Lamalle, M. Lehnen, T. Luce, I. Nunes, A. R. Polevoi, S. D. Pinches, R. A. Pitts, R. Reichle, M. Schneider, J. Snipes, J. van der Laan, G. Vayakis, ITER IRP Contributors, *ITER research plan within the staged approach (Level III - final version)*, Tech. Rep. ITR-24-005, ITER Organization, St Paul-lez-Durance, France (April 2024).  
URL <https://www.iter.org/technical-reports?id=26>
- [2] S. Ishino, Implications of fundamental radiation damage studies in the research and development of materials for a fusion reactor, *Journal of Nuclear Materials* 239 (1996) 24–33. doi:10.1016/S0022-3115(96)00486-2.
- [3] F. Mata, R. Vila, C. Ortiz, N. Casal, A. Ibarra, D. Rapisarda, V. Queral, Analysis of displacement damage in materials in nuclear fusion facilities (DEMO, IMFIF, and TechnoFusion), *Fusion Engineering and Design* 86 (9-11) (2011) 2425–2428. doi:10.1016/j.fusengdes.2010.12.041.
- [4] M. Rubel, Fusion neutrons: Tritium breeding and impact on wall materials and components of diagnostic systems, *Journal of Fusion Energy* 38 (2019) 315–329. doi:10.1007/s10894-018-0182-1.
- [5] A. V. Spitsyn, N. P. Bobyr, T. V. Kulevoy, P. A. Fedin, A. I. Semennikov, V. S. Stolbunov, Use of MeV energy ion accelerators to simulate the neutron damage in fusion reactor materials, *Fusion Engineering and Design* 146 (A) (2015) 1313–1316. doi:10.1016/j.fusengdes.2019.02.065.
- [6] S. Breidokaite, G. Stankunas, Helium production and material damage rate assessment in EU DEMO HCPB divertor, *Radiation Physics and Chemistry* 210 (2023) 111024. doi:10.1016/j.radphyschem.2023.111024.
- [7] L. Li, Y. Hu, L. Peng, J. Shi, Y. Sun, X. Hu, C. Hu, Helium bubble evolution under cascade in bcc iron relevant to fusion conditions investigated by a novel coupling MD-OKMC method, *Journal of Nuclear Materials* 591 (2024) 154908. doi:10.1016/j.jnucmat.2024.154908.
- [8] F. A. Hernández, P. Pereslavtsev, First principles review of options for tritium breeder and neutron multiplier materials for breeding blankets in fusion reactors, *Fusion Engineering and Design* 137 (2018) 243–256. doi:10.1016/j.fusengdes.2018.09.014.
- [9] S. Segantin, R. Testoni, Z. Hartwig, D. Whyte, M. Zucchetti, Optimization of tritium breeding ratio in ARC reactor, *Fusion Engineering and Design* 154 (2020) 111531. doi:10.1016/j.fusengdes.2020.111531.
- [10] J. W. Bae, D. Young, K. Borowiec, V. Badalassi, Integral analysis of the effect of material dimension and composition on tokamak neutronics, *Nuclear Fusion* 64 (5) (2024) 056013. doi:10.1088/1741-4326/ad33ee.
- [11] B. C. Kim, Exploratory neutronic evaluation on the enhancement of tritium breeding and energy multiplication capability using (Th,U)O<sub>2</sub> in a solid-state tritium breeding blanket of a fusion demonstration reactor, *Fusion Engineering and Design* 205 (2024) 114558. doi:10.1016/j.fusengdes.2024.114558.
- [12] V. Prost, S. Ogier-Collin, F. A. Volpe, Compact fusion blanket using plasma facing liquid Li-LiH walls and Pb pebbles, *Journal of Nuclear Materials* 599 (2024) 155239. doi:10.1016/j.jnucmat.2024.155239.
- [13] Z. Ghani, A. Turner, S. Mangham, J. Naish, M. Lis, L. Packer, M. Laughlin, Radiation levels in the ITER tokamak complex during and after plasma operation, *Fusion Engineering and Design* 96-97 (2015) 261–264. doi:10.1016/j.fusengdes.2015.05.019.
- [14] S. C. Wilson, S. W. Mosher, K. E. Royston, C. R. Daily, A. M. Ibrahim, Validation of the MS-CADIS method for full-scale shutdown dose rate analysis, *Fusion Science and Technology* 74 (4) (2018) 288–302. doi:10.1080/15361055.2018.1483687.
- [15] K. Royston, G. Radulescu, W. van Hove, S. Wilson, S. Kim, Assessment of activation on level L3 of the tokamak building due to the ITER tokamak cooling water system, *Fusion Science and Technology* 75 (6) (2019) 458–465. doi:10.1080/15361055.2019.1606519.
- [16] Y. Qiu, M. Ansorge, I. Álvarez, K. Ambrožič, T. Berry, B. Bieńkowska, H. Chohan, A. Čufar, D. Dworak, T. Dezsi, T. Eade, J. García, D. Jimenez-Rey, I. Lengár, A. Lopez-Revelles, V. Lopez, E. Mendoza, F. Mota, M. Martinez-Echevarria, F. Ogando, J. Park, T. Piotrowski, A. Serikov, G. Stankunas, A. Tidikas, G. Tracz, G. Žerovnik, F. Arbeiter, F. Arranz, S. Becerril, P. Cara, D. Bernardi, J. Castellanos, J. Gutiérrez, A. Ibarra, W. Królas, J. Maestre, F. Martín-Fuertes, J. Marugán, G. Micciché, J. Martínez-Serrano, F. Nitti, I. Podadera, U. Wiącek, U. Fischer, Overview of recent advancement in IFMIF-DONES neutronics activities, *Fusion Engineering and Design* 201 (2024) 114242. doi:10.1016/j.fusengdes.2024.114242.
- [17] L. El-Guebaly, P. Wilson, D. Paige, ARIES Team, Initial activation assessment for ARIES compact stellarator power plant, *Fusion Science and Technology* 47 (3) (2005) 440–444. doi:10.13182/FST05-A726.
- [18] R. Pampin, S. Zheng, S. Lilley, B. C. Na, M. J. Laughlin, N. P. Taylor, Activation analyses updating the ITER radioactive waste assessment, *Fusion Engineering and Design* 87 (7-8) (2012) 1230–1234. doi:10.1016/j.fusengdes.2012.02.110.
- [19] Y. Someya, K. Tobita, H. Utoh, N. Asakura, Y. Sakamoto, K. Hoshino, M. Nakamura, S. Tokunaga, Management strategy for radioactive waste in the fusion DEMO reactor, *Fusion Science and Technology* 68 (2) (2017) 423–427. doi:10.1016/j.fusengdes.2012.02.110.
- [20] M. R. Gilbert, T. Eade, C. Bachmann, U. Fischer, N. P. Taylor, Waste assessment of European DEMO fusion reactor designs, *Fusion Engineering and Design* 136 (A) (2018) 42–48. doi:10.1016/j.fusengdes.2017.12.019.
- [21] Q. Cao, X. Wang, M. Yin, S. Qu, L. Zhang, B. Zhou, F. Zhao, Preliminary activation analysis and radioactive waste classification for CFETR, *Fusion Engineering and Design* 172 (2021) 112789. doi:10.1016/j.fusengdes.2021.112789.
- [22] J. Martín-Solís, A. Loarte, M. Lehnen, Formation and termination of runaway beams in ITER disruptions, *Nuclear Fusion* 57 (6) (2017) 066025. doi:10.1088/1741-4326/aa6939.
- [23] O. Vallhagen, O. Embreus, I. Pusztai, L. Hesslow, T. Fülöp, Runaway dynamics in the DT phase of ITER

- operations in the presence of massive material injection, *Journal of Plasma Physics* 86 (4) (2020) 475860401. doi:10.1017/S0022377820000859.
- [24] O. Vallhagen, L. Hanebring, F. J. Artola, M. Lehnen, E. Nardon, T. Fülöp, M. Hoppe, S. L. Newton, I. Pusztai, Runaway electron dynamics in ITER disruptions with shattered pellet injection, *Nuclear Fusion* 64 (8) (2024) 086033. doi:10.1088/1741-4326/ad54d7.
- [25] M. D. Campanell, Negative plasma potential relative to electron-emitting surfaces, *Physical Review E* 88 (3) (2013) 033103. doi:10.1103/PhysRevE.88.033103.
- [26] M. D. Campanell, M. V. Umansky, Strongly emitting surfaces unable to float below plasma potential, *Physical Review Letters* 116 (8) (2016) 085003. doi:10.1103/PhysRevLett.116.085003.
- [27] K. Bradshaw, B. Srinivasan, Energy-dependent implementation of secondary electron emission models in continuum kinetic sheath simulations, *Plasma Sources Science and Technology* 33 (3) (2024) 035008.
- [28] J. A. Kulesza, T. R. Adams, J. C. Armstrong, S. R. Bolding, F. B. Brown, J. S. Bull, T. P. Burke, A. R. Clark, R. A. Forster, III, J. F. Giron, T. S. Grieve, C. J. Josey, R. L. Martz, G. W. McKinney, E. J. Pearson, M. E. Rising, C. J. Solomon, Jr., S. Swaminarayan, T. J. Trahan, S. C. Wilson, A. J. Zukaitis, MCNP<sup>®</sup> code version 6.3.0 theory & user manual, Tech. Rep. LA-UR-22-30006, Los Alamos National Laboratory, Los Alamos, NM, USA (2022). doi:10.2172/1889957.
- [29] A. Kohyama, A. Hishinuma, D. S. G. and R. L. Klueh, W. Dietz, K. Ehrlich, Low-activation ferritic and martensitic steels for fusion application, *Journal of Nuclear Materials* 233-237 (1996) 138–147. doi:10.1016/S0022-3115(96)00327-3.
- [30] G. Federici, W. Biel, M. R. Gilbert, R. Kemp, N. Taylor, R. Wenninger, European DEMO design strategy and consequences for materials, *Nuclear Fusion* 57 (9) (2017) 092002. doi:10.1088/1741-4326/57/9/092002.
- [31] J. W. Bae, E. peterson, J. Shimwell, ARC reactor neutronics multi-code validation, *Nuclear Fusion* 62 (6) (2022) 066016. doi:10.1088/1741-4326/ac5450.
- [32] R. J. Kurtz, K. Abe, V. M. Chernov, D. T. Hoelzer, H. Matsui, T. Muroga, G. R. Odette, Recent progress on development of vanadium alloys for fusion, *Journal of Nuclear Materials* 329-333 (2004) 47–55. doi:doi:10.1016/j.jnucmat.2004.04.299.
- [33] D. Brown, M. Chadwick, R. Capote, A. Kahler, A. Trkov, M. Herman, A. Sonzogni, Y. Danon, A. Carlson, M. Dunn, D. Smith, G. Hale, G. Arbanas, R. Arcilla, C. Bates, B. Beck, B. Becker, F. Brown, R. Casperson, J. Conlin, D. Cullen, M.-A. Descalle, R. Firestone, T. Gaines, K. Guber, A. Hawari, J. Holmes, T. Johnson, T. Kawano, B. Kiedrowski, A. Koning, S. Kopecky, L. Leal, J. Lestone, C. Lubitz, J. M. Damián, C. Mattoon, E. McCutchan, S. Mughabghab, P. Navratil, D. Neudecker, G. Nobre, G. Noguere, M. Paris, M. Pigni, A. Plompen, B. Pritychenko, V. Pronyaev, D. Roubtsov, D. Rochman, P. Romano, P. Schillebeeckx, S. Simakov, M. Sin, I. Sirakov, B. Sleaford, V. Sobes, E. Soukhovitskii, I. Stetcu, P. Talou, I. Thompson, S. van der Marck, L. Welsch-Sherrill, D. Wiarda, M. White, J. Wormald, R. Wright, M. Zerkle, G. Žerovnik, Y. Zhu, ENDF/B-VIII.0: The 8th major release of the nuclear data library with cielo-project cross sections, new standards, and thermal scattering data, *Nuclear Data Sheets* 148 (2018) 1–142. doi:10.1016/j.nds.2018.02.001.
- [34] J. L. Conlin, W. Haec, D. Neudecker, D. K. Parsons, M. C. White, Release of ENDF/B-VIII.0-based ACE data files, Tech. Rep. LA-UR-18-24034, Los Alamos National Laboratory, Los Alamos, NM, United States (May 2018). doi:10.2172/1438139.
- [35] D. E. Cullen, EPICS2014: Electron photon interaction cross sections (version 2014), Tech. Rep. IAEA-NDS-218, International Atomic Energy Agency - Nuclear Data Section, Vienna, Austria (2014).
- [36] H. G. Hughes, Recent developments in low-energy electron/photon transport for MCNP6, *Progress in Nuclear Science and Technology* 4 (2014) 454–458. doi:10.15669/pnst.4.454.
- [37] H. G. Hughes, Improvements in electron-photon-relaxation data for MCNP6, *EPJ Web of Conferences* 153 (2017) 06009. doi:10.1051/epjconf/201715306009.
- [38] M. J. Berger, Electron stopping powers for transport calculations, in: T. Jenkins, W. Nelson, A. Rindi (Eds.), *Monte Carlo Transport of Electrons and Photons*, Plenum Press, New York, NY, 10013, United States of America, 1988, Ch. 3, pp. 57–80. doi:10.1007/978-1-4613-1059-4.
- [39] S. M. Seltzer, Cross sections for bremsstrahlung production and electron-impact ionization, in: T. M. Jenkins, W. R. Nelson, A. Rindi (Eds.), *Monte Carlo Transport of Electrons and Photons*, Plenum Press, New York, NY, 10013, United States of America, 1988, Ch. 4, pp. 81–114. doi:10.1007/978-1-4613-1059-4.
- [40] K. J. Adams, Electron upgrade for MCNP4B, Tech. Rep. LA-UR-00-3581, Los Alamos National Laboratory, Los Alamos, NM, United States (2000).
- [41] M. Chadwick, P. Obložinský, M. Herman, N. Greene, R. McKnight, D. Smith, P. Young, R. MacFarlane, G. Hale, S. Frankle, A. Kahler, T. Kawano, R. Little, D. Madland, P. Moller, R. Mosteller, P. Page, P. Talou, H. Trellue, M. White, W. Wilson, R. Arcilla, C. Dunford, S. Mughabghab, B. Pritychenko, D. Rochman, A. Sonzogni, C. Lubitz, T. Trumbull, J. Weinman, D. Brown, D. Cullen, D. Heinrichs, D. McNabb, H. Derrien, M. Dunn, N. Larson, L. Leal, A. Carlson, R. Block, J. Briggs, E. Cheng, H. Huria, M. Zerkle, K. Kozier, A. Courcelle, V. Pronyaev, S. van der Marck, ENDF/B-VII.0: Next generation evaluated nuclear data library for nuclear science and technology, *Nuclear Data Sheets* 107 (12) (2006) 2931–3118. doi:10.1016/j.nds.2006.11.001.
- [42] D. K. Parsons, Verification of the ENDF7U photonuclear data library for MCNP, Tech. Rep. LA-UR-22-25692, Los Alamos National Laboratory, Los Alamos, NM, United States (June 2022).
- [43] W. B. Wilson, S. T. Cowell, T. R. England, A. C. Hayes, P. Moller, A manual for CINDER'90 version 07.4 codes and data, Tech. Rep. LA-UR-07-8412, Los Alamos National Laboratory, Los Alamos, NM, United States (March 2008).
- [44] C. J. Josey, private communication (April 2024).
- [45] H. Kawamura, E. Ishitsuka, K. Tsuchiya, M. Nakamichi, M. Uchida, H. Yamada, K. Nakamura, H. Ito, T. Nakazawa, H. Takahashi, S. Tanaka, N. Y. S. Kato, Y. Ito, Development of advanced blanket materials for a solid breeder blanket of a fusion reactor, *Nuclear Fusion* 43 (8) (2003) 675–680. doi:10.1088/0029-5515/43/8/306.
- [46] L. V. Boccaccini, F. Arbeiter, P. Arena, J. Aubert, L. Bühler, I. Cristescu, A. Del Novo, M. Eboli, L. Forest, C. Harrington,

- F. Hernandez, R. Knitter, H. Neuberger, D. Rapisarda, P. Sardain, G. A. Spagnuolo, M. Utili, L. Vala, A. Venturini, P. Vladimirov, G. Zhou, Status of maturation of critical technologies and systems design: Breeding blanket, *Fusion Engineering and Design* 179 (2022) 113116. doi:10.1016/j.fusengdes.2022.113116.
- [47] K. Mukai, J.-H. Kim, M. Nakamichi, Measurement of thermal expansion anisotropy in  $\text{be}_{12}\text{ti}$  and  $\text{be}_{12}\text{v}$ , *Nuclear Materials and Energy* 36 (2023) 101473. doi:10.1016/j.nme.2023.101473.
- [48] G. Zhou, F. A. Hernández, P. Pereslvtsev, B. Kiss, A. Retheesh, L. Maqueda, J. H. Park, The European DEMO helium cooled pebble bed breeding blanket: Design status at the conclusion of the pre-concept design phase, *Energies* 16 (14) (2023) 5377. doi:10.3390/en16145377.
- [49] M. Nakamichi, K. J. Hwan, P. Kurinskiy, M. Nakamura, Thermal properties of beryllides as advanced neutron multipliers for DEMO fusion application, *Nuclear Materials and Energy* 15 (2018) 71–75. doi:10.1016/j.nme.2018.02.002.
- [50] Y. Gohar, M. A. Abdou, Neutronic optimization of solid breeder blankets for STARFIRE design, Tech. Rep. CONF-801011-98, Argonne National Laboratory, Argonne, IL, USA (January 1980). URL [https://inis.iaea.org/search/search.aspx?orig\\_q=RN:12630669](https://inis.iaea.org/search/search.aspx?orig_q=RN:12630669)
- [51] M. Dalle Donne, S. Dorner, D. F. Lupton, Fabrication and properties of  $\text{Zr}_5\text{Pb}_3$ , a new neutron multiplier material for fusion blankets, *Journal of Nuclear Materials* 141-143 (1) (1986) 369–372. doi:10.1016/S0022-3115(86)80067-8.
- [52] R. Gaisin, P. Pereslvtsev, S. Baumgaertner, L. Seemann, E. Gaisina, V. Chakin, S. Udartsev, P. Vladimirov, B. Gorr, Lanthanum plumbide as a new neutron multiplier material, *Journal of Materials Research and Technology* 24 (2023) 3399–3412. doi:10.1016/j.jmrt.2023.03.211.
- [53] X. Gao, J. Wang, W. Lu, Y. Lu, D. Chu, W. Wang, Lithium lead titanate ( $\text{Li}_2\text{Pb}_x\text{Ti}_{1-x}\text{O}_3$ ,  $0.1 < x < 0.9$ ): A new tritium-neutron complex breeder for fusion reactor blanket, *Journal of Nuclear Materials* 599 (2024) 155240. doi:10.1016/j.jnucmat.2024.155240.
- [54] M. N. Rosenbluth, S. V. Putvinski, Theory for avalanche of runaway electrons in tokamaks, *Nuclear Fusion* 37 (10) (1997) 1355–1362. doi:10.1088/0029-5515/37/10/I03.
- [55] L. Hesslow, O. Embréus, O. Vallhagen, T. Fülöp, Influence of massive material injection on avalanche runaway generation during tokamak disruptions, *Nuclear Fusion* 59 (8) (2019) 084004. doi:10.1088/1741-4326/ab26c2.
- [56] J. Martín-Solís, A. Loarte, M. Lehnen, Runaway electron dynamics in tokamak plasmas with high impurity content, *Physics of Plasmas* 22 (9) (2015) 092512. doi:10.1063/1.4931166.
- [57] G. D. Hobbs, J. A. Wesson, Heat flow through a Langmuir sheath in the presence of electron emission, *Plasma Physics* 9 (1) (1967) 85–87. doi:10.1088/0032-1028/9/1/410.
- [58] R. Chodura, Plasma-wall transition in an oblique magnetic field, *Physics of Fluids* 25 (1982) 1628–1633. doi:10.1063/1.863955.
- [59] P. C. Stangeby, The Chodura sheath for angles of a few degrees between the magnetic field and the surface of divertor targets and limiters, *Nuclear Fusion* 52 (8) (2012) 083012. doi:10.1088/0029-5515/52/8/083012.
- [60] N. A. Garland, H.-K. Chung, C. J. Fontes, M. C. Zammit, J. Colgan, T. Elder, C. J. McDevitt, T. M. Wildey, X.-Z. Tang, Impact of a minority relativistic electron tail interacting with a thermal plasma containing high-atomic-number impurities, *Physics of Plasmas* 27 (4) (2020) 040702. doi:10.1063/5.0003638.

Supplementary data for the article entitled:  
Large radiation back-flux from Monte Carlo simulations of fusion  
neutron-material interactions

Michael A. Lively<sup>a,b,\*</sup>, Danny Perez<sup>a</sup>, Blas P. Uberuaga<sup>c</sup>, Yanzeng Zhang<sup>a</sup>, Xian-Zhu Tang<sup>a</sup>

<sup>a</sup>*Theoretical Division, Los Alamos National Laboratory, Los Alamos, NM, 87545, United States of America*

<sup>b</sup>*X Computational Physics Division, Los Alamos National Laboratory, Los Alamos, NM, 87545, United States of America*

<sup>c</sup>*Materials Science and Technology Division, Los Alamos National Laboratory, Los Alamos, NM, 87545, United States of America*

---

**Abstract**

In this supplement, we provide plots of all major data sets obtained during this work, which are tabulated in an abbreviated format in the main manuscript. The plotted data include energy-resolved distributions of the total radiation back-fluxes, operating-time-resolved integrated delayed back-fluxes, and some relevant neutron cross sections which are useful to interpret these data. These plots will be useful and informative to readers who seek greater detail on some points or those who wish to replicate or extend this work.

---

---

\*This work was supported by the U.S. Department of Energy Office of Fusion Energy Sciences (DOE-FES) [grant number 89233218CNA000001].

\*Corresponding author.

*Email addresses:* [livelym@lanl.gov](mailto:livelym@lanl.gov) (Michael A. Lively), [danny\\_perez@lanl.gov](mailto:danny_perez@lanl.gov) (Danny Perez), [blas@lanl.gov](mailto:blas@lanl.gov) (Blas P. Uberuaga), [yzengzhang@lanl.gov](mailto:yzengzhang@lanl.gov) (Yanzeng Zhang), [xtang@lanl.gov](mailto:xtang@lanl.gov) (Xian-Zhu Tang)

## Total radiation back-fluxes

Energy distributions for neutron, gamma ray, and electron back-fluxes are plotted in Figs. S1–S4 for all material configurations studied in this work.

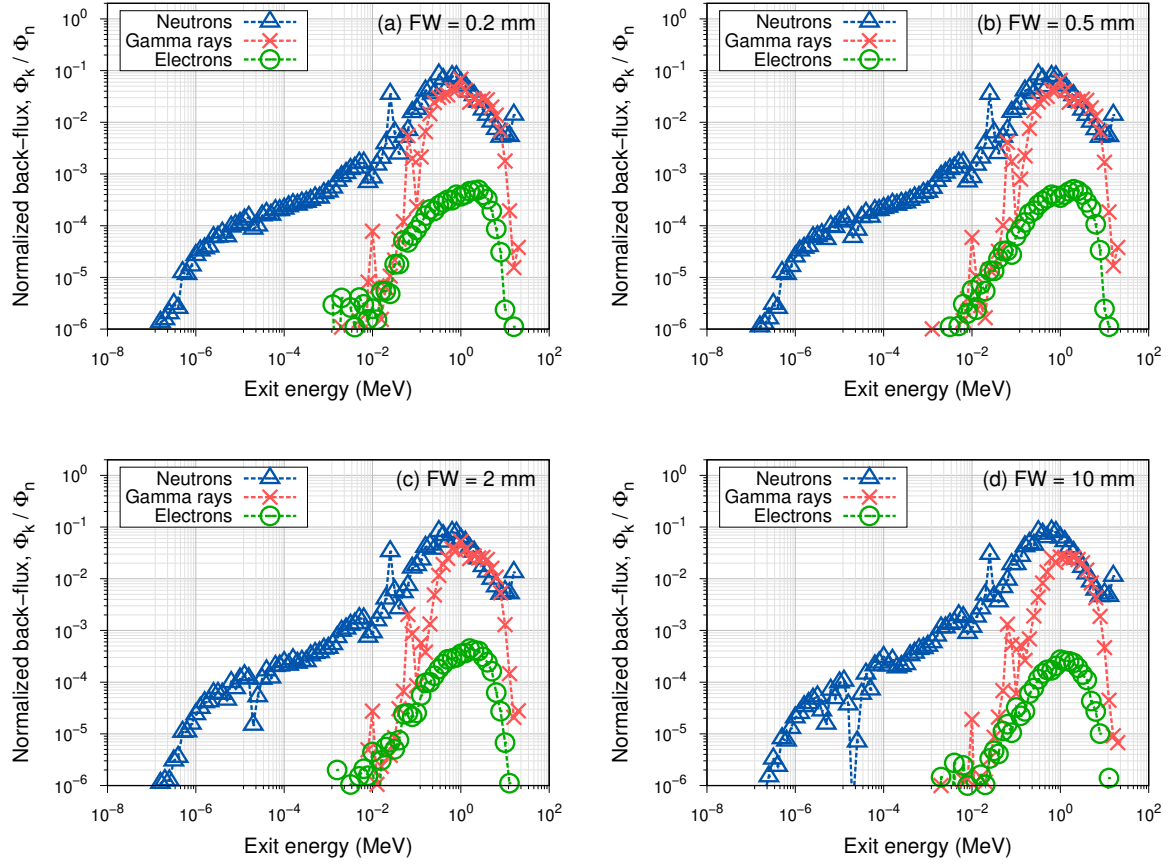


**Fig. S1.** Energy-resolved, time-integrated radiation back-fluxes of neutrons, gamma rays, and relativistic electrons for iron structural material with tungsten first wall thicknesses of (a) 0.2 mm, (b) 0.5 mm, (c) 2 mm, and (d) 10 mm.

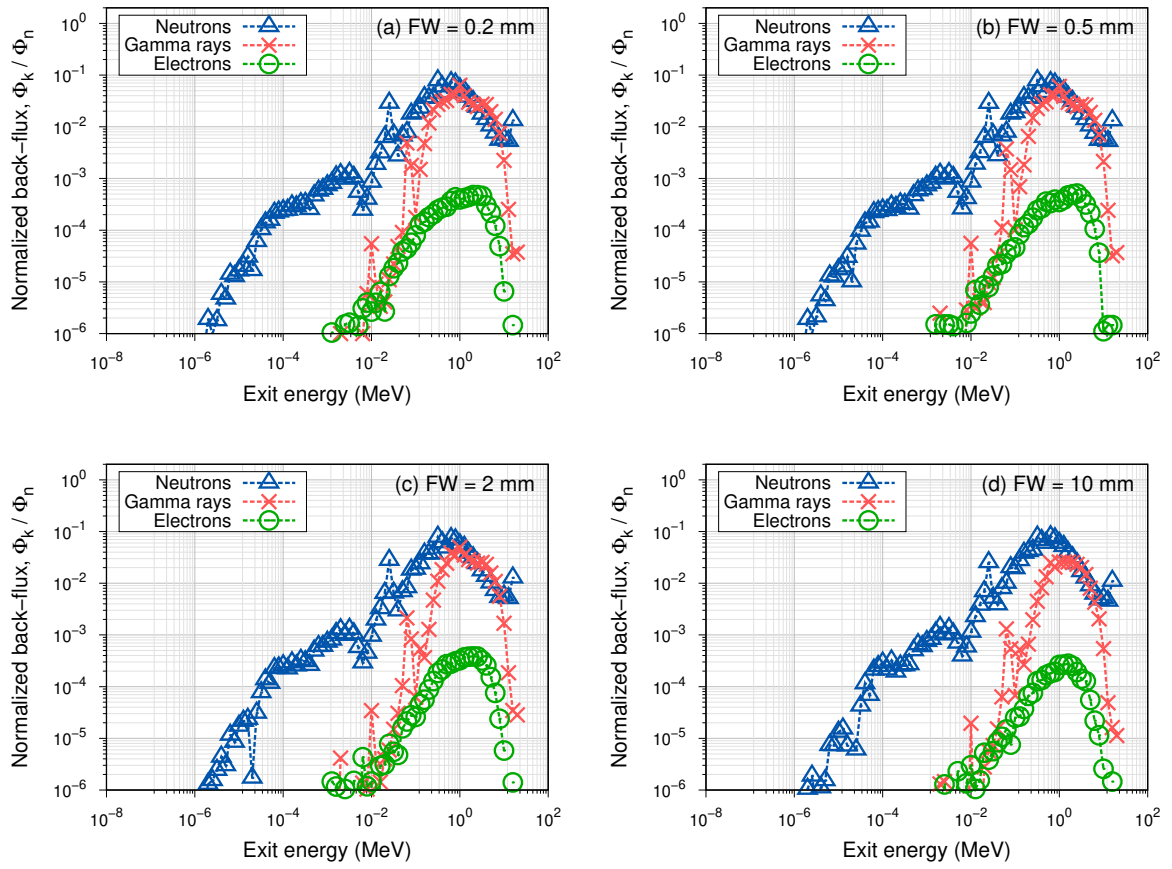


**Fig. S2.** Energy-resolved, time-integrated radiation back-fluxes of neutrons, gamma rays, and relativistic electrons for RAFM steel structural material with tungsten first wall thicknesses of (a) 0.2 mm, (b) 0.5 mm, (c) 2 mm, and (d) 10 mm.

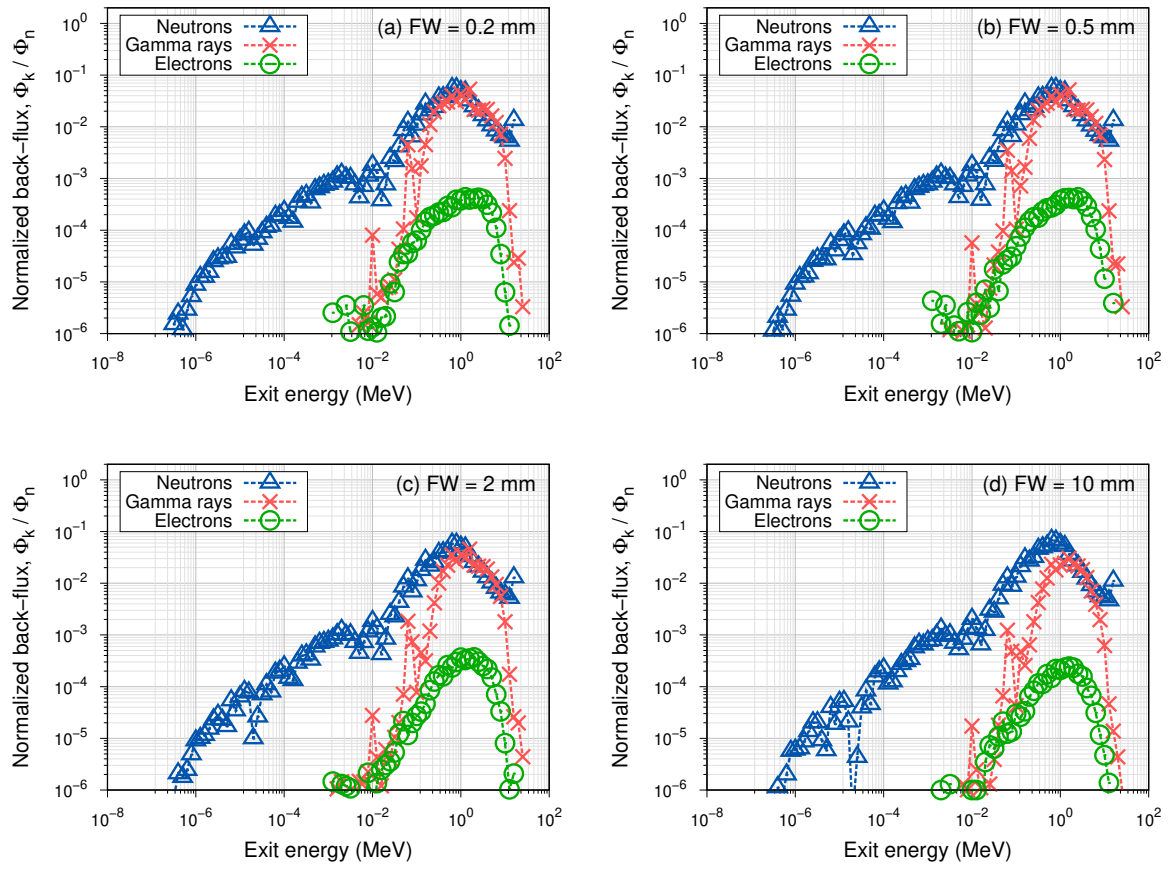


**Fig. S3.** Energy-resolved, time-integrated radiation back-fluxes of neutrons, gamma rays, and relativistic electrons for Inconel 718 structural material with tungsten first wall thicknesses of (a) 0.2 mm, (b) 0.5 mm, (c) 2 mm, and (d) 10 mm.

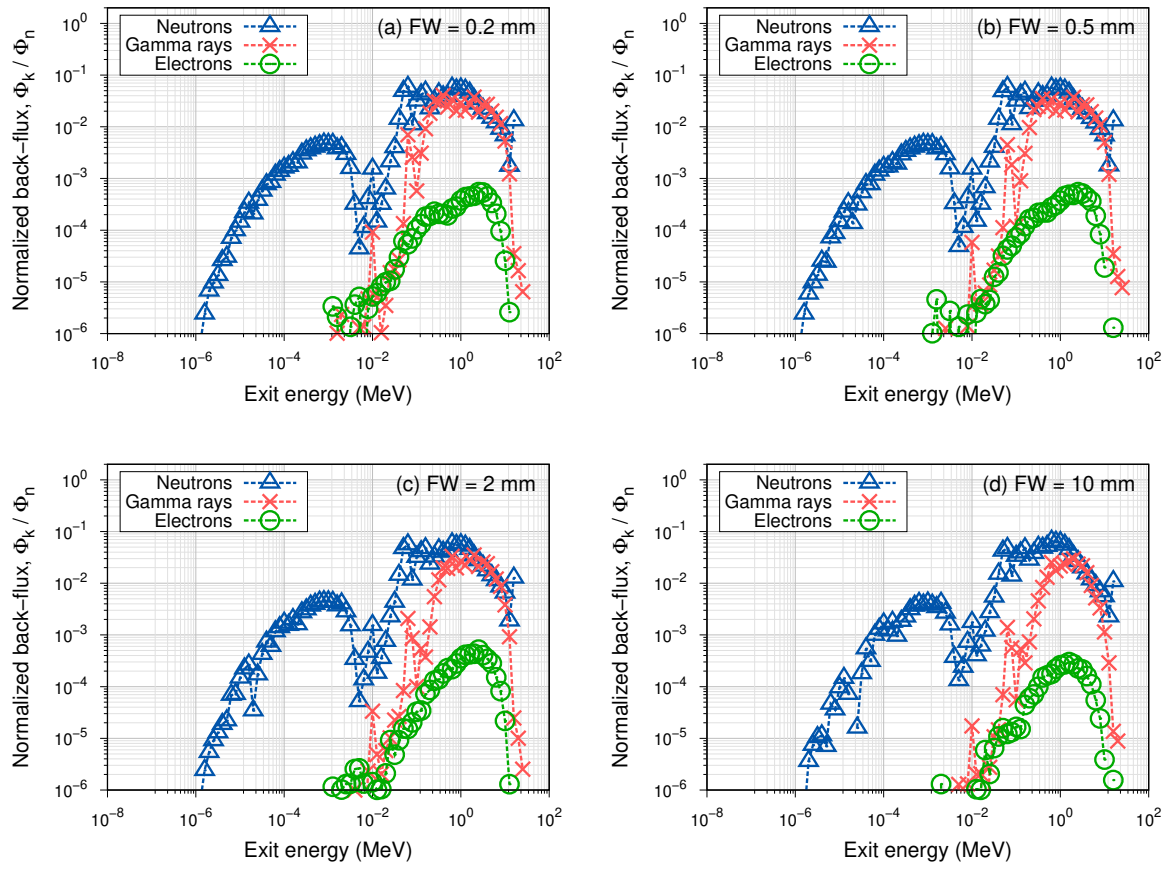


**Fig. S4.** Energy-resolved, time-integrated radiation back-fluxes of neutrons, gamma rays, and relativistic electrons for V-4Ti-4Cr structural material with tungsten first wall thicknesses of (a) 0.2 mm, (b) 0.5 mm, (c) 2 mm, and (d) 10 mm.



Cosine distributions for neutron, gamma ray, and electron back-fluxes are plotted in Figs. S5–S8 for all material configurations studied in this work.

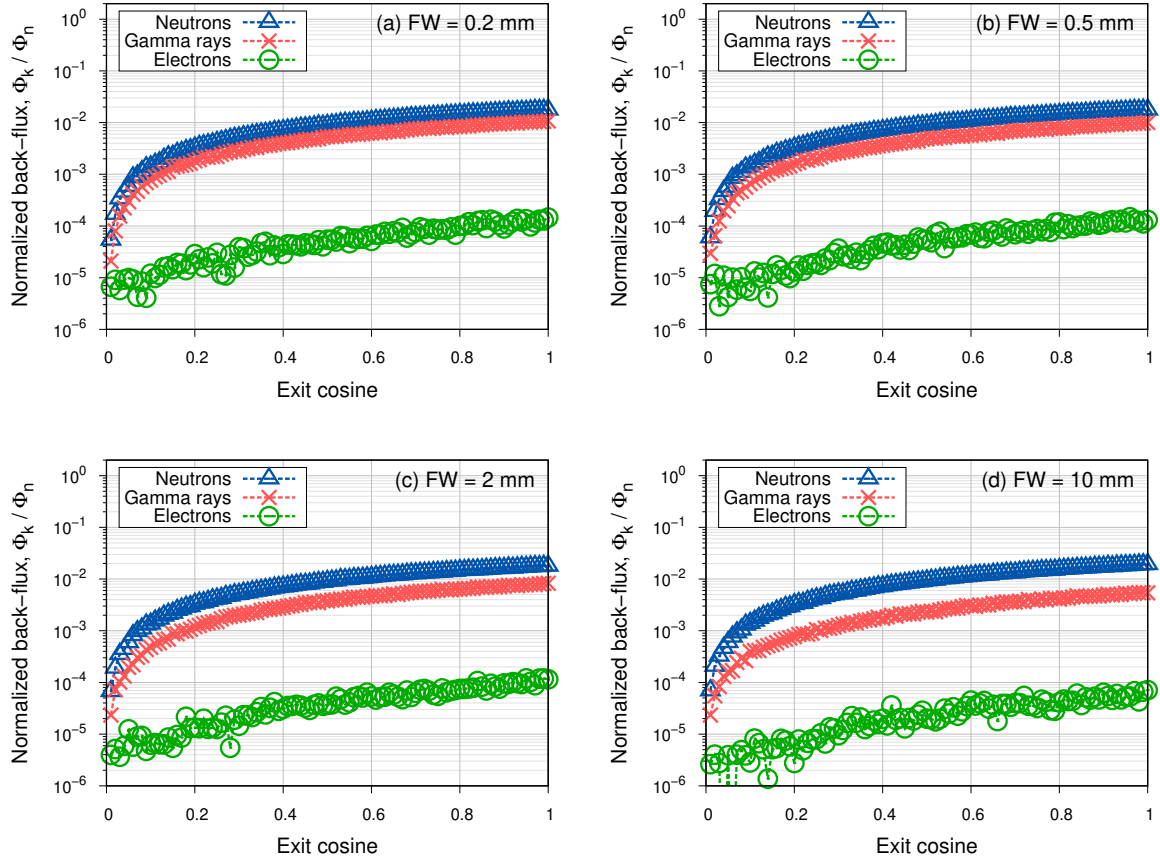


**Fig. S5.** Cosine-resolved, time-integrated radiation back-fluxes of neutrons, gamma rays, and relativistic electrons for iron structural material with tungsten first wall thicknesses of (a) 0.2 mm, (b) 0.5 mm, (c) 2 mm, and (d) 10 mm.

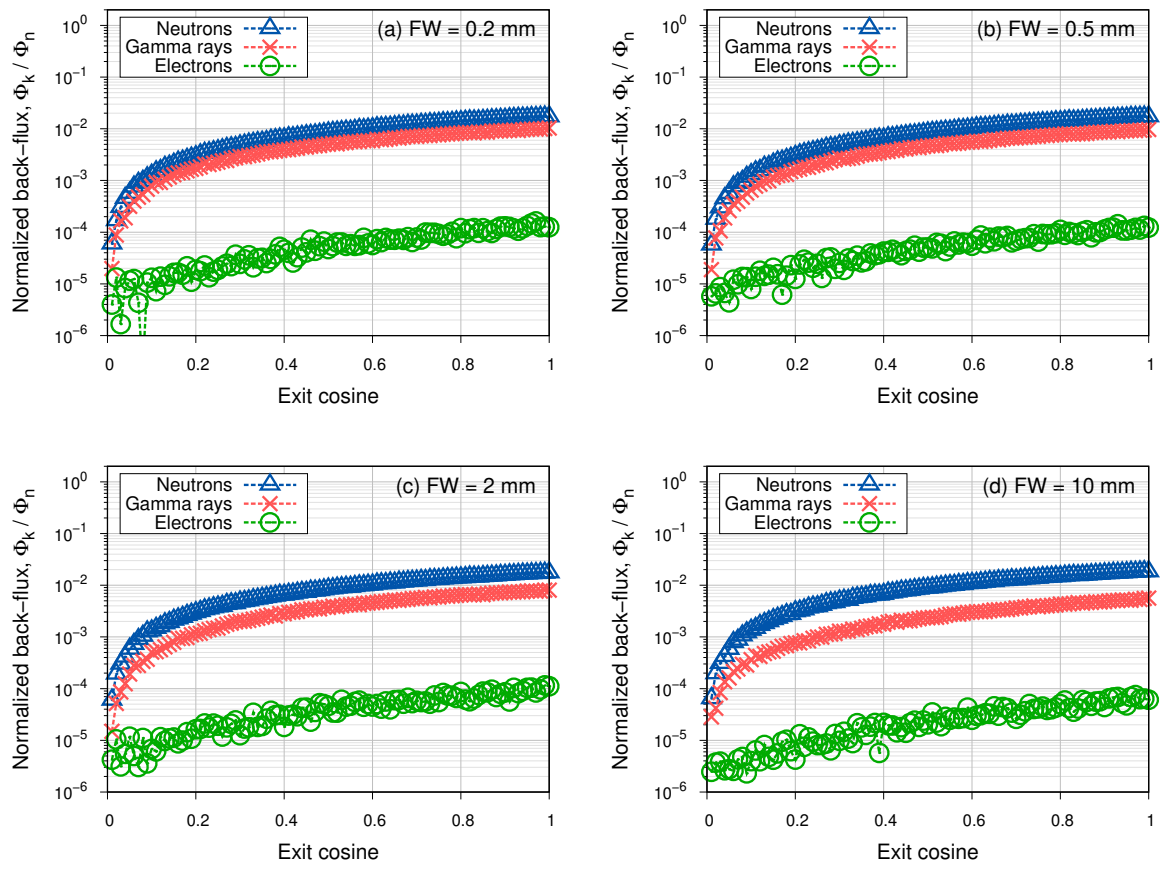


**Fig. S6.** Cosine-resolved, time-integrated radiation back-fluxes of neutrons, gamma rays, and relativistic electrons for RAFM steel structural material with tungsten first wall thicknesses of (a) 0.2 mm, (b) 0.5 mm, (c) 2 mm, and (d) 10 mm.

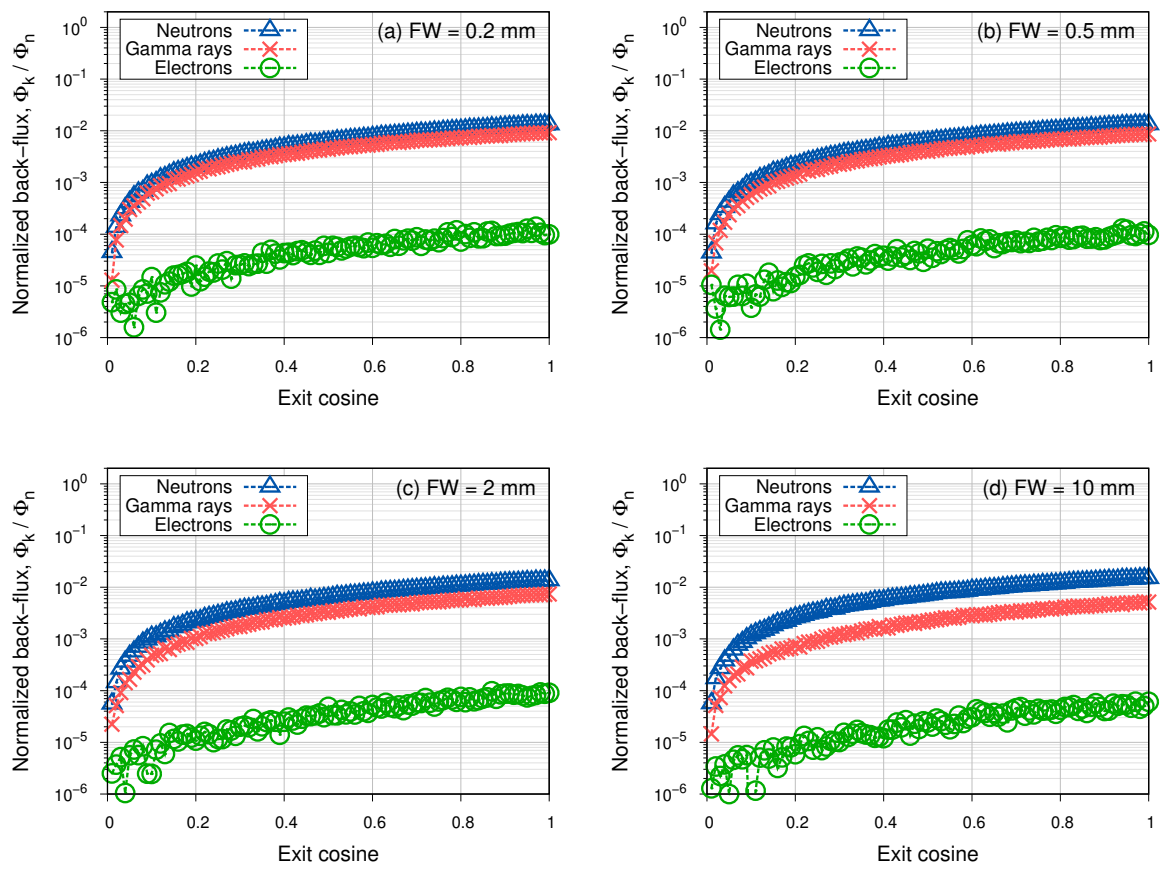


**Fig. S7.** Cosine-resolved, time-integrated radiation back-fluxes of neutrons, gamma rays, and relativistic electrons for Inconel 718 structural material with tungsten first wall thicknesses of (a) 0.2 mm, (b) 0.5 mm, (c) 2 mm, and (d) 10 mm.

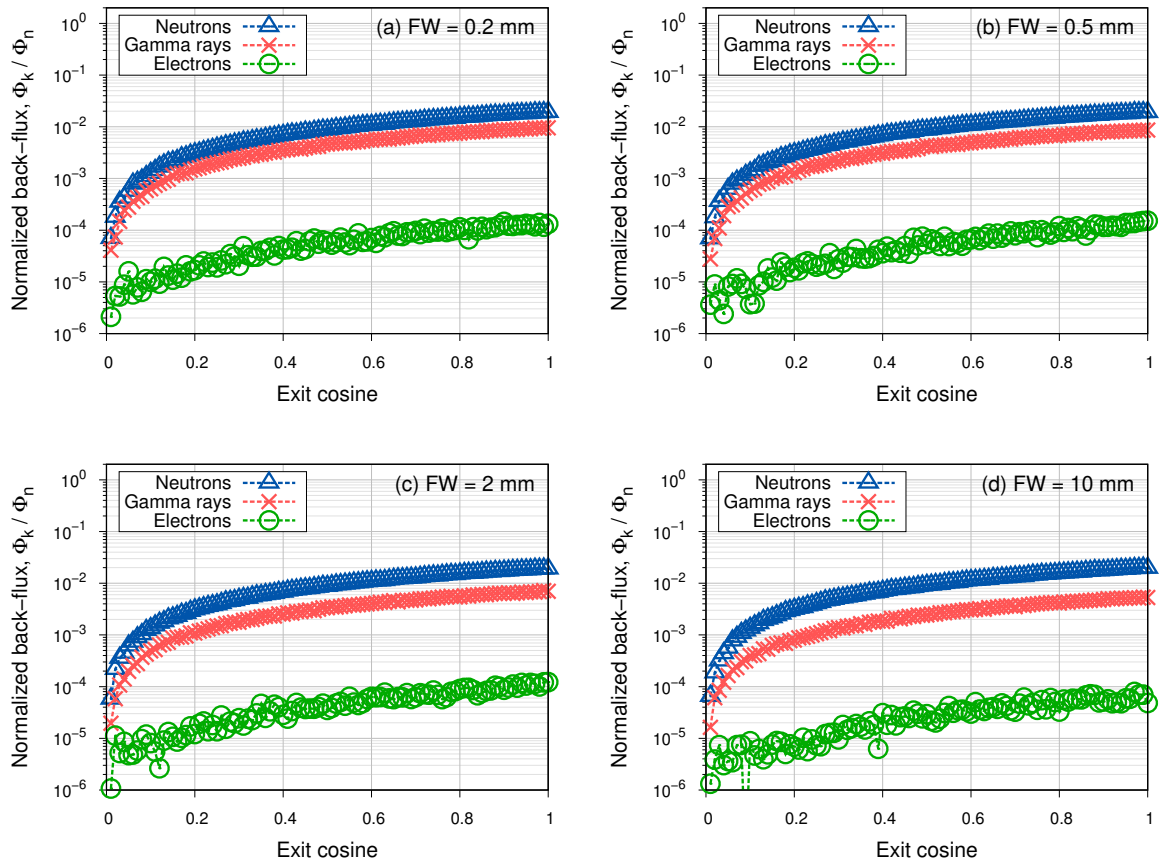


**Fig. S8.** Cosine-resolved, time-integrated radiation back-fluxes of neutrons, gamma rays, and relativistic electrons for V-4Ti-4Cr structural material with tungsten first wall thicknesses of (a) 0.2 mm, (b) 0.5 mm, (c) 2 mm, and (d) 10 mm.

## Time-integrated delayed back-fluxes

Time-integrated delayed back-fluxes for gamma rays and electrons are plotted in Figs. S9–S12 for all material configurations studied in this work.

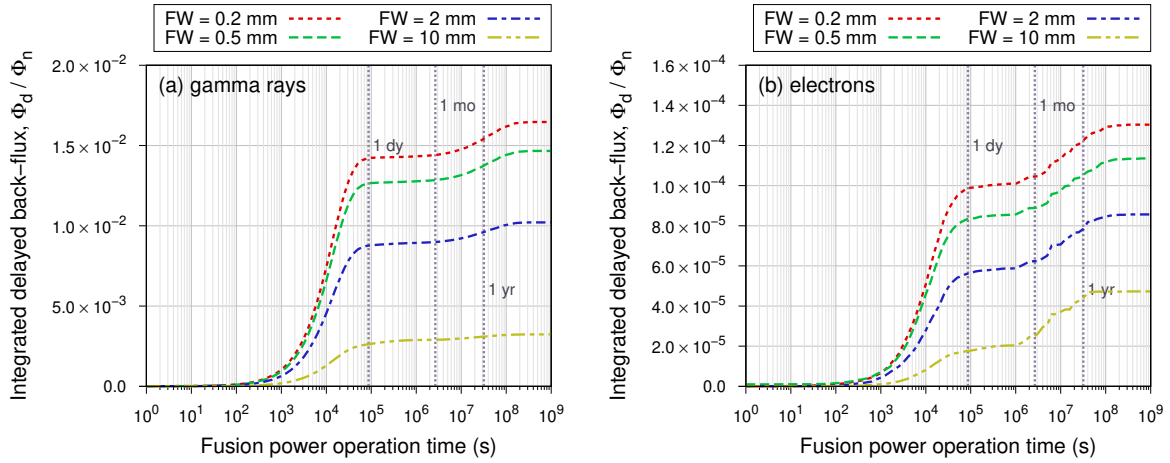


**Fig. S9.** Time-integrated delayed back-fluxes of (a) gamma rays and (b) electrons for different first wall thicknesses with iron structural material.

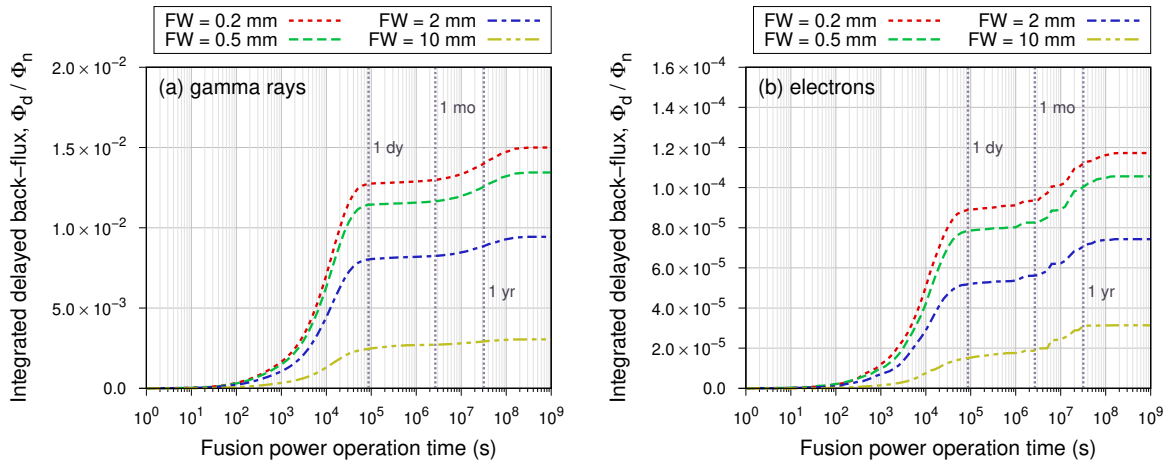


**Fig. S10.** Time-integrated delayed back-fluxes of (a) gamma rays and (b) electrons for different first wall thicknesses with RAFM steel structural material.

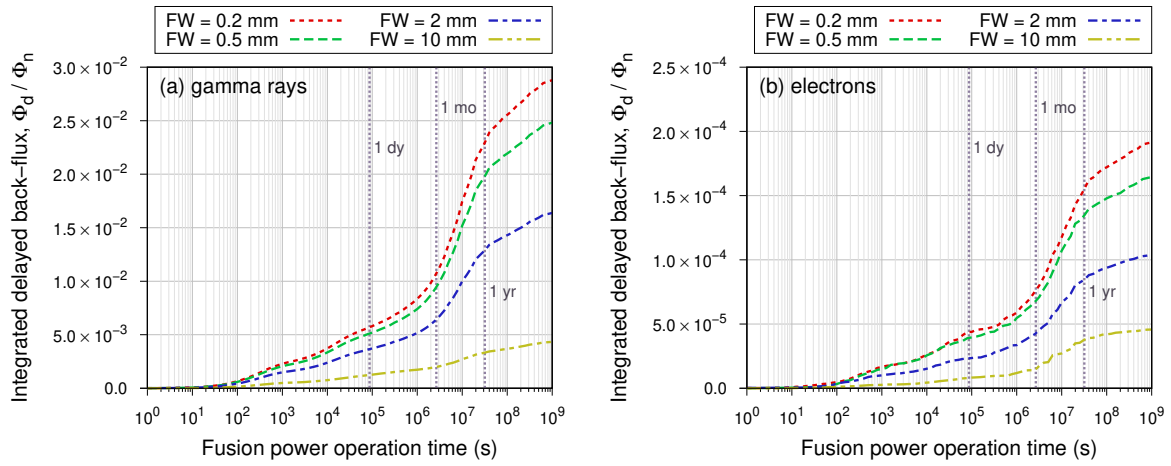


**Fig. S11.** Time-integrated delayed back-fluxes of (a) gamma rays and (b) electrons for different first wall thicknesses with Inconel 718 structural material.

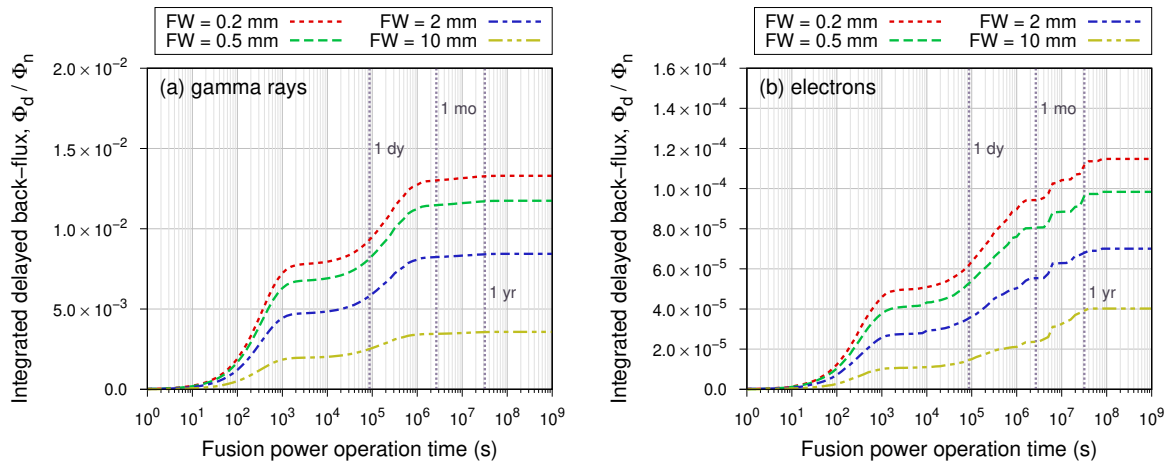


**Fig. S12.** Time-integrated delayed back-fluxes of (a) gamma rays and (b) electrons for different first wall thicknesses with V-4Ti-4Cr structural material.

## Neutron cross sections

The following relevant cross sections are plotted here:

- Total cross section,  $\sigma_t$ : the total probability for a neutron to interact with an atom of the material.
- Neutron multiplication cross section,  $\sigma_m$ : the weighted probability for a neutron collision to generate additional neutrons, evaluated as

$$\sigma_m = \sum_{k=1}^{N_k} X_k \sigma_k \quad (\text{S9})$$

where  $\sigma_k$  is a reaction which might produce secondary neutrons and  $X_k$  is the number of secondary neutrons produced, which may be energy-dependent. In general, a larger ratio  $\sigma_m/\sigma_t$  indicates that a neutron in a material is more likely to generate secondary neutrons before losing energy or being captured.

- Secondary neutron energy probability distribution functions (PDFs) at various incident neutron energies above the threshold for  $\sigma_m$ .

Cross sections and secondary neutron energy PDFs for a given material are the weighted sum of the per-isotope cross sections and PDFs. These data were extracted from the ENDF/B-VIII.0 library in ACE format used by MCNP with the ACETk package (<https://github.com/njoy/ACETk>).

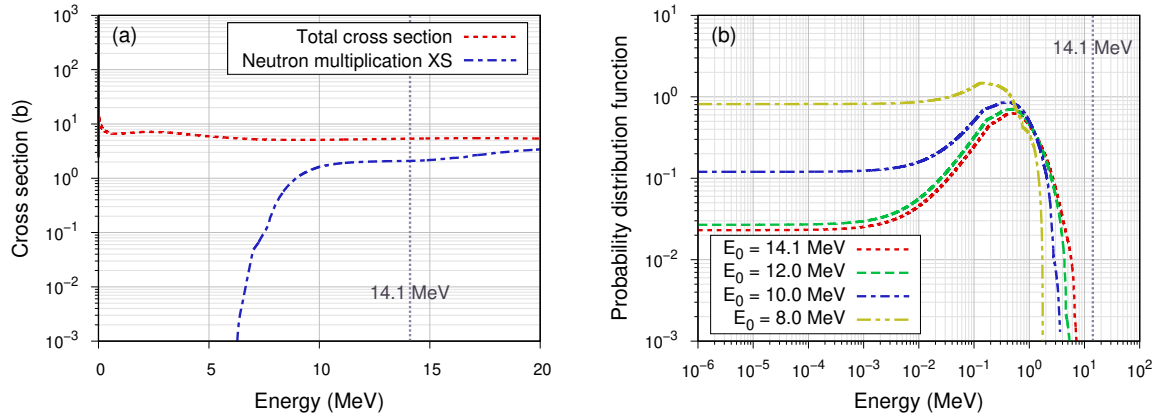


**Fig. S13.** Neutron cross section data for tungsten: (a) Total and neutron multiplication cross sections. (b) Secondary neutron energy probability distribution functions for various incident neutron energies. Dashed vertical lines indicate the 14.1 MeV fusion neutron energy as a useful reference point.

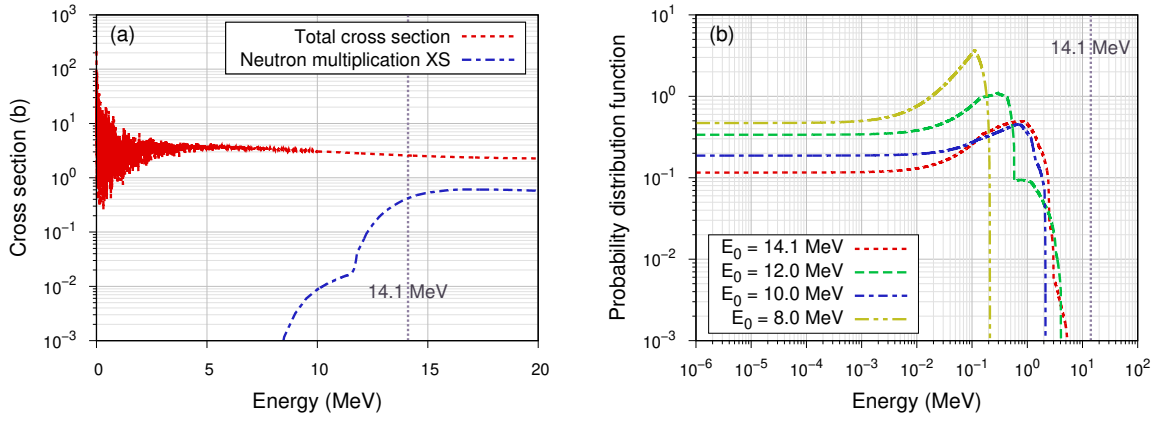


**Fig. S14.** Neutron cross section data for iron: (a) Total and neutron multiplication cross sections. (b) Secondary neutron energy probability distribution functions for various incident neutron energies. Dashed vertical lines indicate the 14.1 MeV fusion neutron energy as a useful reference point.

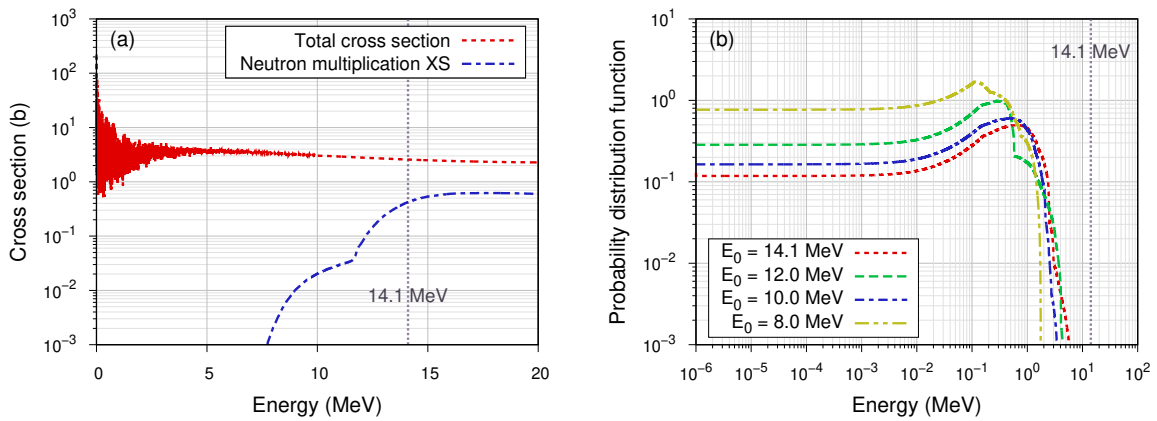


**Fig. S15.** Neutron cross section data for RAFM steel: (a) Total and neutron multiplication cross sections. (b) Secondary neutron energy probability distribution functions for various incident neutron energies. Dashed vertical lines indicate the 14.1 MeV fusion neutron energy as a useful reference point.



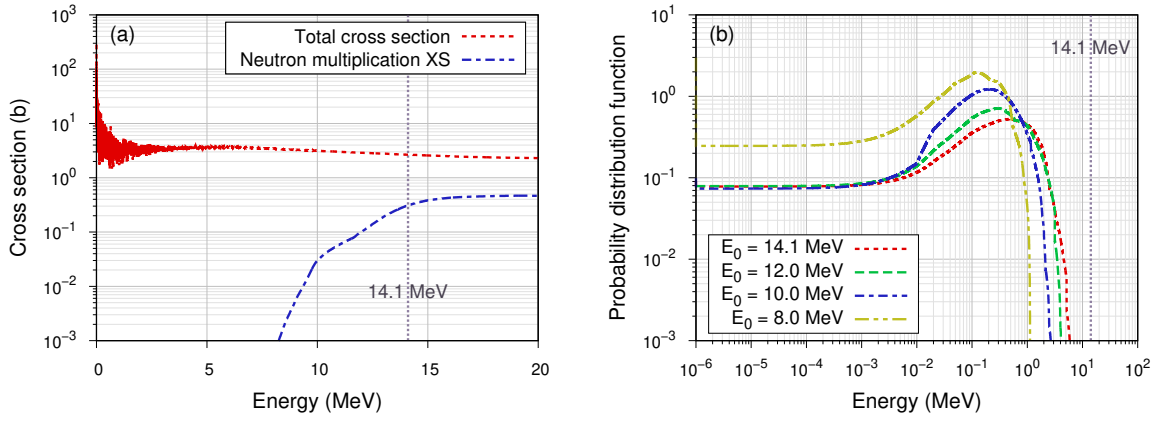


**Fig. S16.** Neutron cross section data for Inconel 718: (a) Total and neutron multiplication cross sections. (b) Secondary neutron energy probability distribution functions for various incident neutron energies. Dashed vertical lines indicate the 14.1 MeV fusion neutron energy as a useful reference point.

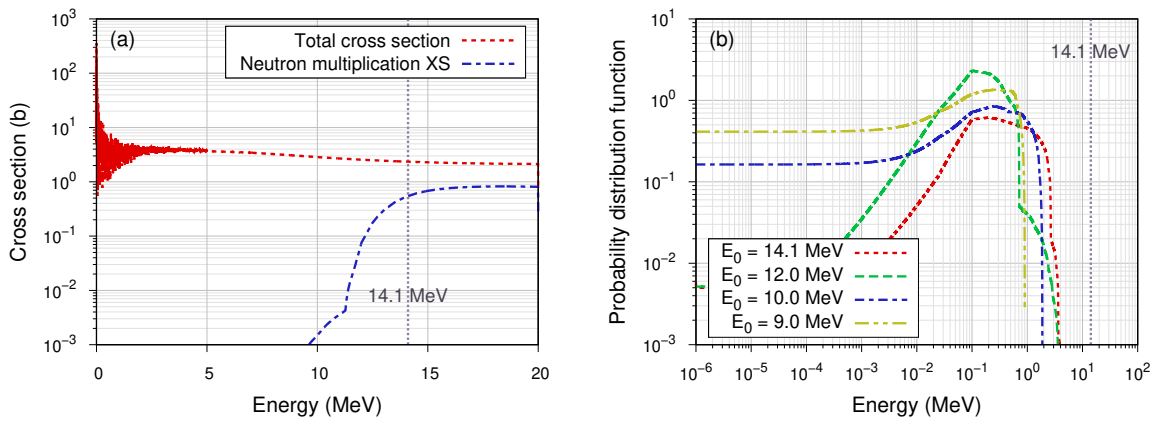


**Fig. S17.** Neutron cross section data for V-4Ti-4Cr: (a) Total and neutron multiplication cross sections. (b) Secondary neutron energy probability distribution functions for various incident neutron energies. Dashed vertical lines indicate the 14.1 MeV fusion neutron energy as a useful reference point.